

## The Thermal Structure of Titan's Atmosphere

CHRISTOPHER P. MCKAY, JAMES B. POLLACK, AND RÉGIS COURTIN<sup>1</sup>

*Space Science Division, NASA Ames Research Center, Moffett Field, California 94035*

Received January 25, 1988; revised November 9, 1988

**We have developed a radiative–convective model of the thermal structure of Titan's atmosphere. The model computes the solar and infrared radiation in a series of spectral intervals with vertical resolution. Sources of opacity in the visible and near infrared include stratospheric haze particles, methane cloud particles, and gaseous methane; sources of opacity in the thermal infrared include the pressure-induced opacity of  $N_2$ ,  $CH_4$ , and  $H_2$ , the permitted transitions of  $C_2H_2$  and  $C_2H_6$ , and particulate opacity. The haze properties are determined with a simple microphysics model. The model contains a minimum of free parameters and we try to determine these by fits to independent data sets. We find that gas and haze opacity alone, with the temperatures fixed by Voyager observations, produces a model that is within a few percent of radiative convective balance everywhere in the atmosphere. In a self-consistent computation of temperatures, we find that our model calculation for the surface temperature is, in general, colder than the observed value by 5–10°K. The presence or absence of methane condensation clouds only slightly alters the results. Good agreement can be obtained by adjusting the parameters in the model. The model parameters in these optimized cases are typically within 15% of the baseline values and within the limits allowed by observations. We conclude that the most important factors controlling Titan's thermal structure are absorption of sunlight by the stratospheric haze and the pressure-induced gas opacity in the infrared. Within the uncertainties of the model, these effects can explain the observed temperature profile. Condensation clouds play a minor role, if any.** © 1989 Academic Press, Inc.

The Voyager flyby of the Saturn system provided a good definition of the composition and temperature structure of Titan's atmosphere. The surface temperature was determined to be near 95°K (Lindal *et al.* 1983), implying a greenhouse warming of a little over 10°K above the effective temperature of emission to space. The temperature declines to a minimum of ~70°K at 40 km while higher in the atmosphere the temperature increases, reaching 170°K in the stratosphere.

In this paper we report on a detailed model of the thermal structure of Titan's atmosphere. Our primary goal is to determine if the observed thermal structure, including the 10°K greenhouse effect, can be

adequately explained with known gaseous and haze opacities or alternatively if the presence of a significant tropospheric methane cloud layer or other absorption is required.

The major component of Titan's atmosphere is  $N_2$  with a few percent  $CH_4$  and trace amounts of other hydrocarbons (Kunde *et al.* 1981). The high altitude haze observed on Titan (Rages *et al.* 1983, Rages and Pollack 1983) is most likely photochemically produced organic solid material (see, e.g., Khare *et al.* 1984, Sagan and Thompson 1984). Based on data from the Voyager Infrared Spectrometer (IRIS), Samuelson *et al.* (1981) have suggested that there is ~10% Ar, although a recent analysis of the data with improved absorption coefficients by Toon *et al.* (1988) has suggested that this may not be the case. Voyager observations

<sup>1</sup> Permanent address: Laboratoire d'Astronomie Infra-Rouge, Observatoire de Paris-Meudon, France.

have indicated that the present Titan atmosphere is close to radiative equilibrium, with a convective zone only at the lower few kilometers of the atmosphere (Lindal *et al.* 1983, Eshleman *et al.* 1983, Flasar 1983).

Samuelson (1983) provided a brief review of pre-Voyager models of Titan's thermal structure and developed an analytical radiative equilibrium model that was vertically homogeneous and considered the radiation balance in three broad spectral intervals. His results confirmed pre-Voyager suggestions that the temperature inversion observed on Titan was the result of strong stratospheric absorption of solar ultraviolet and penetration to near the surface of longer wavelength solar visible radiation (see, e.g., Danielson *et al.* 1973, Pollack 1973). Samuelson suggested the presence of enhanced opacity in the regions near 500 (~20 km) and 30 mb (~65 km), which he attributed to possible condensation clouds of  $\text{CH}_4$  and  $\text{C}_2\text{H}_2$ - $\text{C}_2\text{H}_6$ - $\text{C}_3\text{H}_8$ , respectively. He also identified the region from 400 to 600  $\text{cm}^{-1}$  as the thermal infrared "window" region, a spectral region of low optical depth that limits the greenhouse effect on Titan. We have extended this work by developing a detailed numerical model with spectral and vertical resolution coupled to a microphysical model of the stratospheric haze.

Our overall approach to modeling the thermal structure of Titan's atmosphere is to develop a model with as few adjustable parameters as possible and to restrict these parameters to specific independent physical quantities. For example, we treat the haze production rate as an adjustable parameter but we use a simple microphysics model to compute the haze size and density as a function of altitude once the haze production is specified. Hence the vertical distribution of haze particle size and density are not free parameters in our computation of the temperature profile. We use spacecraft and ground-based data sets (but not the observed temperature structure) to choose values for these adjustable parameters.

Thus, the thermal balance and the radiative-convective temperature profile can be computed with essentially no free parameters. We later adjust these parameters to optimize the fit to the observed temperature profile.

We use the model of the thermal structure of Titan's atmosphere in two separate ways. First we use this model with the temperature profile fixed to the Voyager egress temperature data. In this mode we investigate the effects of various parameters (whose values are chosen to satisfy constraints placed by other data sets) on radiative fluxes and the thermal balance. Second, we compute equilibrium radiative-convective temperature profiles for comparison to the observed temperature distribution.

The likelihood of condensate clouds in the lower atmosphere of Titan is poorly understood and there is some disagreement on the most probable nature and extent of any such clouds (Thompson and Sagan 1984, Samuelson 1983, Toon *et al.* 1988). We explore the possibility that the thermal structure of the atmosphere can be used to infer tropospheric cloud properties.

Finally we attempt to closely match the Voyager temperature profile by altering the model parameters from their values determined from the observational data sets. We present two optimized cases, one with a methane condensation cloud and one without. As far as possible we adjust the model parameters in such a way that the fit to the observational data sets is still fairly good. We find that our model calculation for the surface temperature is, in general, colder than the observed value. The addition of methane condensation clouds does not result in a significantly improved fit. Good agreement can be obtained by adjusting the parameters in the model, within the limits allowed by observations.

#### BASELINE NO-CLOUD CASE AND NOMINAL CLOUD CASE

The radiative transfer techniques, the spectral intervals, and the other details of

the model are described in the Appendix. The haze properties are derived from a microphysics model and the results are shown in Figs. 1–4. As described in the Appendix the haze model is determined primarily by the geometric albedo of Titan (see Figs. 5 and 6), while the methane, hydrogen, and cloud levels in the model are constrained by the Voyager IRIS data (see Figs. 7–9).

Since we are interested in the effect of clouds and other putative absorbers on the temperature profile of Titan's atmosphere we must first define a baseline case which is without any such effects. We refer to this case as the baseline no-cloud case to emphasize the fact that it does not contain any condensation clouds. As will be seen below this baseline no-cloud case provides a reasonably good fit to Titan's temperature profile, particularly if the methane distribution is held fixed to the values determined from the Voyager data. For this reason the diagnostic studies we have performed on the radiative energy transport and thermal balance have been based on the baseline no-cloud model. We feel that this case represents a good model of Titan's atmosphere.

To include the effects of clouds we define a nominal cloud case, in which the properties of the cloud are based on the results of Toon *et al.* (1988). In this case a methane cloud is inserted in the model in all layers in which methane is at its saturation vapor pressure (from  $\sim 5$  to 30 km). The cloud particles are all the same size with a radius of 100  $\mu\text{m}$ . The optical depth of the nominal cloud is 2, specified at 200  $\text{cm}^{-1}$ . The opacity of the nominal cloud is distributed proportional to the gaseous methane concentration within each saturated layer.

While the two cases listed above are the primary ones used in this paper and will be referred to frequently, we have also considered several other cases. In particular we consider methane condensation clouds with particles over the size range 0.1–200  $\mu\text{m}$ . In addition we consider a no-cloud case and a cloud case optimized to match the Voyager temperature profile.

For the baseline no-cloud case, the nominal cloud case, and the two optimized cases the adjustable parameters in the model are determined independently to give a good fit to the observational data sets. The particular combination of values that gives a good fit may not be unique.

#### ADJUSTABLE PARAMETERS

The adjustable parameters that must be chosen to complete the baseline no-cloud and the nominal cloud models are listed in Table I. There are nine parameters that specify physical quantities in the baseline model; five of these (charging radius, pressure level of production, visible absorption scale factor, and infrared absorption scale factor) are related to the haze, two are related to the composition of the atmosphere (the  $\text{CH}_4$  relative humidity and the  $\text{H}_2$  mixing ratio), and the remaining two are the surface reflectance in the visible and in the infrared. When methane clouds are included in the model two additional parameters are introduced, the particle size and the cloud opacity at a reference wavelength. In addition, when we consider optimizing the fit of the model results to the voyager temperature data we will introduce four other adjustments to the model (see Table III). With the exception of the adjustments factor to the  $\text{CH}_4\text{--N}_2$  absorption coefficient, there is no physical basis for choosing these additional adjustments—they are chosen to help produce a close fit between the model results and the Voyager temperature data.

The numerical values of parameters and the data set that is used to choose values for the baseline (9 parameters) and nominal cloud (11 parameters) models are listed in Table I. These data sets include (1) high phase angle images of Titan (Rages and Pollack 1983, Rages *et al.* 1983), (2) the Voyager IRIS spectra (Samuelson *et al.* 1981), and (3) Earth-based observations of the geometric albedo of Titan (Neff *et al.* 1984, 1985, Fink and Larson 1979). In the following paragraphs we describe the fitting pro-

TABLE I  
MODEL ADJUSTABLE PARAMETERS

Variable	No-cloud baseline	Nominal cloud	Constraint
Charging radius, $r_c$	$0.09\text{ }\mu\text{m}$	$0.09\text{ }\mu\text{m}$	Rages <i>et al.</i> (1983), see Fig. 1
Pressure of haze production, $P_o$	$10^{-4}\text{ mb}$	$10^{-4}\text{ mb}$	Rages and Pollack (1983), <sup>b</sup> see Fig. 2
Haze production rate, $C_o$	$0.35^a$	$0.35^a$	Geometric albedo, see Figs. 5 and 6
Haze visible absorption factor, $X_v$	$\frac{4}{3}$	$\frac{4}{3}$	Geometric albedo, see Figs. 5 and 6
Haze infrared absorption factor, $X_i$	0.5	0.5	IRIS data, see Fig. 7
Surface relative humidity, $RH_{CH_4}$	60%	60%	IRIS data, see Fig. 7 <sup>c</sup>
H <sub>2</sub> mixing ratio, $f_{H_2}$	0.3%	0.3%	IRIS data, see Fig. 7 <sup>c</sup>
Visible surface reflectance, $A_v$	0.1	0	Geometric albedo, see Figs. 5 and 6
Infrared surface reflectance, $A_{ir}$	0	0	No constraint
Methane cloud particle radius, $r_c$	—	$100\text{ }\mu\text{m}$	IRIS data, see Fig. 7 <sup>c</sup>
Opacity of cloud at $200\text{ cm}^{-1}$ , $\tau_c$	—	2	IRIS data, see Fig. 7 <sup>c</sup>

<sup>a</sup> In units of  $3.5 \times 10^{-14}\text{ g cm}^{-2}\text{ sec}^{-1}$ .  
<sup>b</sup> Only weakly constrained by the Rages and Pollack results. Equally good fits are obtained for any  $P_o < 0.1\text{ mb}$ .  
<sup>c</sup> A comparison to the IRIS data is shown in Fig. 7; see Toon *et al.* (1988) for detailed comparisons.

cedure using the baseline no-cloud case as the example.

The parameter  $r_c$  which controls the particle charging effects is chosen based primarily on constraints on particle sizes near optical depth unity. Size estimates of Titan's aerosols based on Voyager high-phase-angle images by Rages *et al.* (1983) suggest that in the upper few tenths of an optical depth in Titan's atmosphere the cross-section-averaged particle radius lies between  $0.2$  and  $0.5\text{ }\mu\text{m}$ . This range of values is shown as the crosshatched region in Fig. 1. Also shown, by the continuous line, is the recommended radius distribution of Tomasko and Smith (1982) based on polarimetry data as modified by West *et al.* (1983). A choice of  $r_c = 0.09\text{ }\mu\text{m}$  represents the baseline value for this parameter and the resulting values for the radius are shown by squares. To pass within the crosshatched region in Fig. 1,  $r_c$  must be between  $0.05$  and  $0.15\text{ }\mu\text{m}$ . Borucki *et al.* (1987) have recently developed a theoretical model of particle charging in Titan's upper atmosphere from which they conclude that the number of charges per particle is approximately 30 times the radius of the

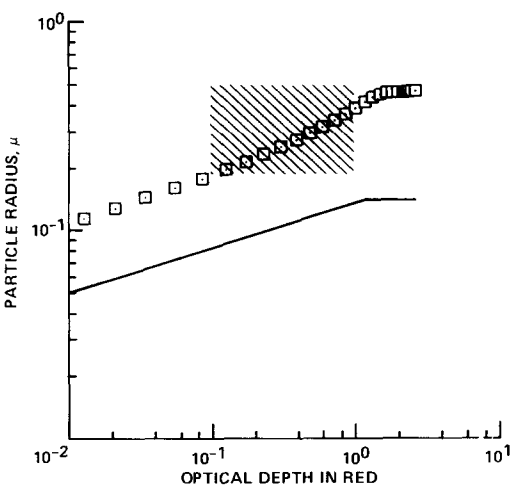


FIG. 1. Comparison of the particle size in the baseline haze model, shown in Fig. 3, to the limits determined by Rages *et al.* (1983) from size estimates of Titan's aerosols based on Voyager high-phase-angle images. This range of values is shown as the crosshatched region and the baseline haze model results are shown as squares at each computation point in the model. Also shown as an unmarked solid line is the recommended radius distribution of Tomasko and Smith (1982) based on polarimetry data with the suggested modification of West *et al.* (1983). The horizontal axis is the optical depth at  $0.64\text{ }\mu\text{m}$ .

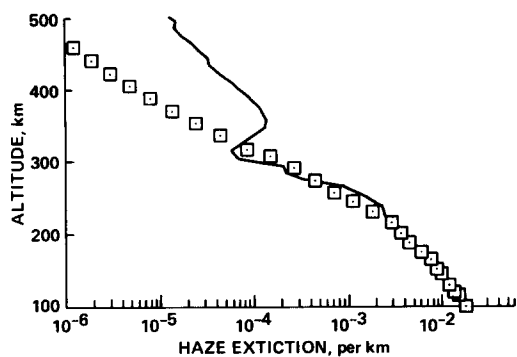


FIG. 2. Comparison of the high altitude extinction properties of the baseline haze, shown in Fig. 3, to the extinction values of Rages and Pollack (1983). The Rages and Pollack values are shown as the solid line; the square markers are the model calculations.

particle in micrometers. The value of  $r_c$  is inversely proportional to the square of the charge per unit radius (see Eq. A18 of Turco *et al.* 1982); a value of  $r_c$  of  $0.09 \mu\text{m}$  corresponds to  $\sim 16$  charges on a  $1\text{-}\mu\text{m}$  radius particle.

As shown in Fig. 2, the altitude of the production of haze is chosen to yield an upper atmospheric extinction profile (squares) that is in reasonable agreement with the extinction values of Rages and Pollack (1983) (solid line). The simple aerosol model used here does not attempt to accurately model the high altitude distribution of the haze. This has little effect on the main haze layer; in model calculations the altitude and particle size at optical depth unity (at  $0.64 \mu\text{m}$ ) were unchanged as the pressure of maximum haze production is varied from  $10^{-1}$  to  $10^{-4}$  mb. This is expected from previous model's of haze particles on Titan (Toon *et al.* 1980, Pollack *et al.* 1980). Following Toon *et al.* (1980), we set  $P_y = P_o/3$ .

The particle radius, number density, relative production rate, and optical depth profile (at  $0.63 \mu\text{m}$ ) of the haze particles obtained for the values of the haze parameters listed for the cases considered in Table I are shown in Fig. 3. In Fig. 4 the wavelength dependence of the optical properties of the

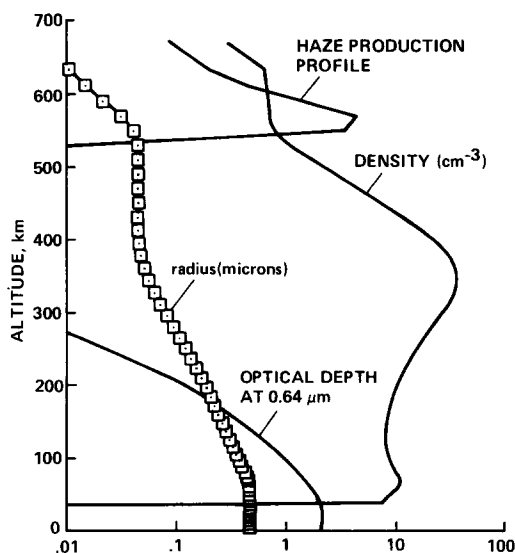


FIG. 3. Particle size, number density, relative production rate, and optical depth at  $0.64 \mu\text{m}$  for the haze model defined by the baseline no-cloud case (see Table I; a production rate of  $C_o = 0.35(\times 3.5 \times 10^{-14} \text{ g cm}^{-2} \text{ sec}^{-1})$ , a production maximum at  $P_o = 10^{-4}$  mb, and a charge radius of  $r_c = 0.09 \mu\text{m}$ . The markers on the radius curve show the computation points used in the haze model.

haze is shown at the altitude corresponding to optical depth unity in the haze for each spectral interval. The solid, dashed, and dotted lines are the asymmetry factor,  $\langle \theta \rangle_h$ , the single scattering albedo,  $\bar{\omega}_h$ , and the al-

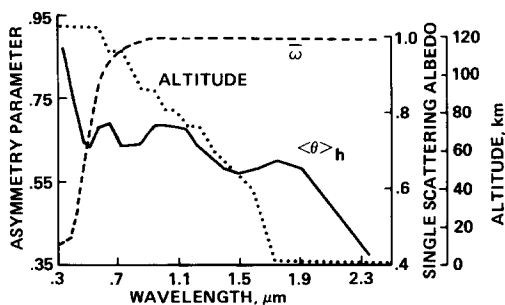


FIG. 4. The wavelength dependence of the optical properties of the haze. The solid and dashed lines are the asymmetry factor,  $\langle \theta \rangle_h$ , and the single scattering albedo,  $\bar{\omega}_h$  of the haze at the altitude corresponding to haze optical depth unity. This altitude is plotted as the dotted line.

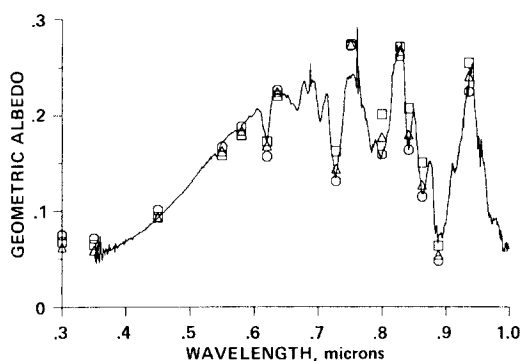


FIG. 5. The geometric albedo of the baseline no-cloud model shown as individual open squares at the wavelengths used in the computation. The wavelengths and the methane absorption coefficients used in the calculation are listed in Table IV. The solid curve is the data of Neff *et al.* (1984) corrected for the size of the optical disk of Titan as described in the text. The geometric albedo data are used to choose values of the following model parameters: the haze production rate ( $C_0$ ), the surface reflectance ( $A_v$ ), and the haze absorption scale factor in the visible ( $X_v$ ). The baseline values for these parameters are listed in Table I. The geometric albedo of the optimized no-cloud model is shown as circles. The model parameters used in the calculation are listed in Table III. Also shown are the geometric albedo values (triangles) of the optimized cloud model (Table II, case 5a). The model parameters used in the calculation are listed in Table III.

titude of haze optical depth unity,  $\tau_h$ , respectively, for the haze. The decrease in the asymmetry factor with increasing wavelength and the change from absorbing to scattering particles is expected since the ratio of particle size to wavelength is becoming smaller and more Rayleigh-like and Rayleigh scattering has zero asymmetry. In addition the index of refraction of the particles is decreasing sharply with increasing wavelength (Khare *et al.* 1984, as discussed below) causing the shift to scattering ( $\bar{\omega} = 1$ ).

Data on the geometric albedo of Titan's atmosphere over the wavelength range 0.3 to 1.0  $\mu\text{m}$  have been tabulated by Neff *et al.* (1984) and extended to 2.5  $\mu\text{m}$  by Neff *et al.* (1985) and Fink and Larson (1979). The Neff *et al.* (1984) data are shown by the continuous curve in Fig. 5 (multiplied by

the factor  $(2560/2850)^2$  to correct for the optical radius of Titan, as suggested by Smith *et al.*, manuscript in preparation). We have chosen several wavelengths at which to do monochromatic calculations of the geometric albedo that can be compared to the data. These calculations utilize monochromatic absorption coefficients of methane, listed in Table III, both in the continuum and in the methane bands. The monochromatic absorption coefficients are in general quite different from the exponential sums used to compute the broadband transmissions for the solar energy deposition calculations (see, e.g., Pollack *et al.* 1986). We use the observed geometric albedo to constrain three model parameters: the surface visible albedo, the haze optical properties and the haze production rate. We also consider the effect of altering the particle charge,  $r_c$ , on the geometric albedo but we have already chosen this parameter as described above. The smaller size distribution of Tomasko and Smith (1982), shown in Fig. 1, does not yield a good fit to the albedo data.

The visible region of the spectrum between 0.3 and 0.6  $\mu\text{m}$  is free of significant methane absorption and scattering by the haze particles determines the geometric albedo; thus this region is ideal for determining the optical properties of the haze. Since the haze is above most of the atmosphere Rayleigh scattering is negligible; it becomes important at wavelengths shorter than  $\sim 0.3 \mu\text{m}$ . In the region of the spectrum from 0.7 to 1.0  $\mu\text{m}$  there is significant methane absorption as well as scattering by the haze. In this region the altitude distribution of the haze in relation to the distribution of the methane determines the contrast in the geometric albedo in the methane bands. In our model altering the haze production rate alters the balance between scattering by the haze, which tends to increase the albedo, and methane absorption, which tends to lower the albedo. Thus, this region of the spectrum is used to determine the haze production rate. Beyond 1  $\mu\text{m}$  the haze optical depth falls off and the geometric albedo be-

comes sensitive to the surface albedo. We have used the maximum values of the geometric albedo reported in the region of 1–2  $\mu\text{m}$ , corresponding to minimum methane absorption, to determine the values of the surface reflectance. These data, at  $\lambda = 1.1, 1.3, 1.5,$  and  $2.1 \mu\text{m}$ , are from Fink and Larson (1979) and are shown in Fig. 6.

In determining the optical properties of the haze, our initial approach was to follow the procedure of Rages and Pollack (1979) and independently choose the values of the imaginary index of refraction for each of the low methane absorption "continuum" points to agree with the observations. When we did this, the results, with the ex-

ception of the 0.75- $\mu\text{m}$  point, were similar in form to the tholin optical constants reported by Khare *et al.* (1984) from 0.3 to 0.9  $\mu\text{m}$ . The values at 0.75  $\mu\text{m}$  were highly suspect since the methane absorption coefficient for this wavelength was obtained by extrapolation from the room temperature values which may be inappropriate for this wavelength (L. Giver, personal communication). Overall, we found that the Neff *et al.* (1984) data are well matched by setting the haze imaginary index of refraction to a value  $\frac{4}{3}$  times larger than that reported by Khare *et al.* (1984) and using their real index unchanged. The possible physical significance of this adjustment is not clear.

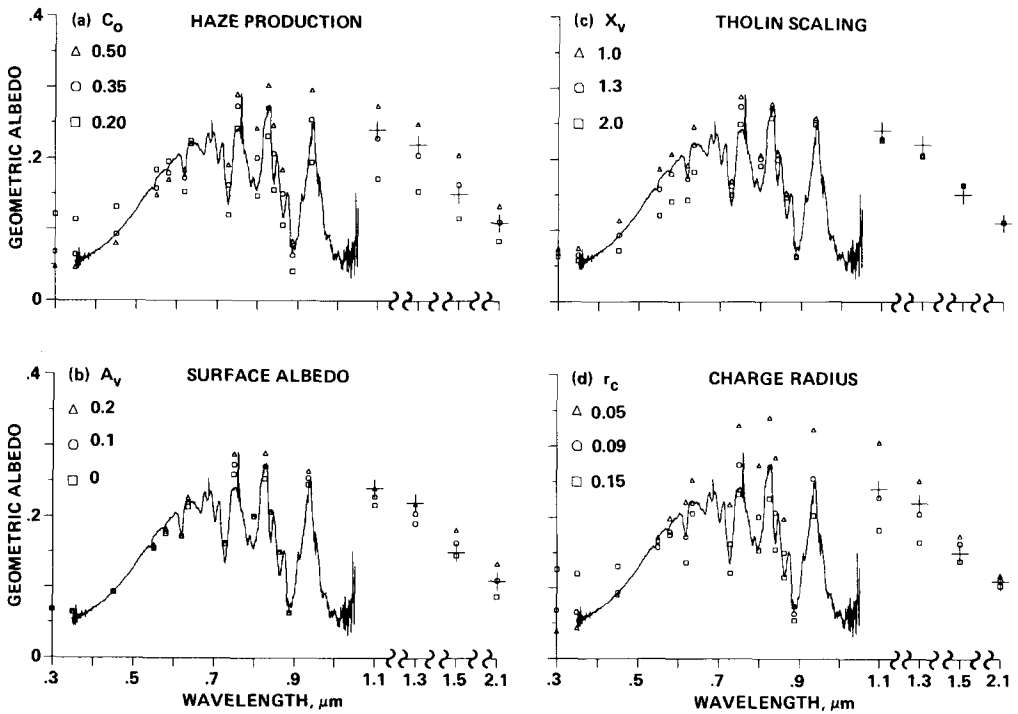


FIG. 6. The same as Fig. 5 except that each of the model parameters determined from the geometric albedo data are varied to illustrate the degree to which the data constrain the baseline values listed in Table I. The crosses at the wavelengths of 1.1, 1.3, 1.5, and 2.1  $\mu\text{m}$  are the data from Fink and Larson (1979). In (a), the haze production rate ( $C_0$ ) is varied from 0.2 to 0.5 about the baseline value of 0.35 (in units of  $3.5 \times 10^{-14} \text{ g cm}^{-2} \text{ sec}^{-1}$ ). In (b), the surface reflectance ( $A_v$ ) varies from 0 to 0.2; its baseline value is 0.1. The absorption coefficient of the haze in the visible is determined by scaling the results of Khare *et al.* (1984) by a constant factor ( $X_v$ ). In (c), this scaling factor is varied from unity to 2; the baseline value is  $\frac{4}{3}$ . In (d), the charge radius,  $r_c$ , is varied from 0.5 to 0.15  $\mu\text{m}$ , about the baseline value of 0.09  $\mu\text{m}$ .

The advantage of this procedure over fitting each individual continuum point is that it is possible to extend our values of the optical properties to the 1- to 2- $\mu\text{m}$  region. In addition, the good agreement obtained by merely scaling the tholin optical constant suggests that tholin is a good compositional analog for the Titan haze particles. Thus in the thermal infrared region of the spectrum we use a similar scaling approach to determine the haze index of refraction.

The best fit of the haze model to the geometric albedo data of Neff *et al.* (1984) is shown by the circles in Fig. 5. Figures 6a, 6b, 6c, and 6d illustrate the sensitivity of the computed albedo spectrum to the values for the haze production rate, the surface albedo, the tholin optical scaling factor, and the charge radius, respectively. In each case, variations from the baseline values of 0.35 (units of  $3.5 \times 10^{-14} \text{ g cm}^{-2} \text{ sec}^{-1}$ ), 0.1,  $\frac{4}{3}$ , and 0.09  $\mu\text{m}$ , respectively, are studied.

Another important data set that can be used to constrain model parameters is the Voyager IRIS spectrum from 200 to 600  $\text{cm}^{-1}$ . This data set includes thermal brightness temperatures and limb to center intensity ratios. Several authors have shown that this data set can be used, together with the thermal structure of the atmosphere to determine the hydrogen mixing ratio, the surface methane concentration, and the properties of the haze (Samuelson *et al.* 1981, Courtin 1982, Thompson and Sagan 1984, Toon *et al.* 1988). Toon *et al.* (1988) have reviewed the recent developments in this approach and our values are similar to their results. In particular, we find that a surface relative humidity of 60% and the hydrogen mixing ratio of 0.3% provide the best fits to the IRIS data. Our results are in agreement with those of Toon *et al.* (1988) and Thompson and Sagan (1984). Because these cases are identical to the discussion in Toon *et al.* (1988) our results for methane and hydrogen are only summarized here.

To achieve the correct emission temperature in the region of 600  $\text{cm}^{-1}$  (and, at the

same time, constraining the haze production rate by the geometric albedo) it is necessary to adjust the haze thermal infrared optical properties (Toon *et al.* 1988). This is done by scaling the Khare *et al.* optical constants. A reasonable fit to the emission spectra is obtained by using a scaling factor of  $\frac{1}{2}$ . This is shown in the bottom curve of Fig. 7. The emission calculations shown in Fig. 7 correspond to the two-stream source function method (Toon *et al.* 1989, 1977) based upon the hemispheric-constant two stream model (Pollack and McKay 1985) at

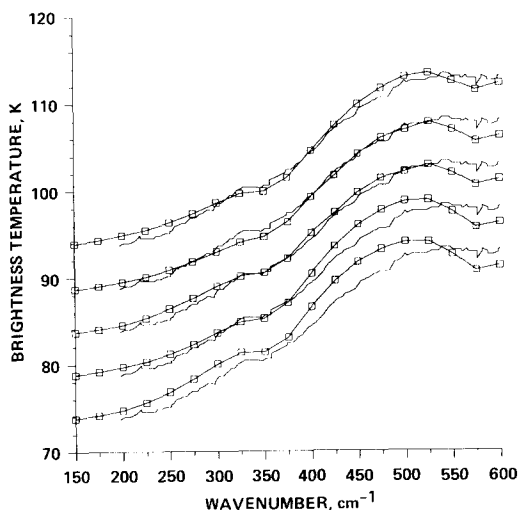


FIG. 7. Comparison of the IRIS brightness temperature data (solid unmarked line) at 57° with the model predictions for the baseline no-cloud model (bottom set of curves, the model points are the open circles). The temperature profile is set by the Voyager egress data as described in the text. The second from the bottom set of curves is for the baseline no-cloud case but with the  $\text{CH}_4\text{-N}_2$  pressure induced absorption coefficients of Courtin (1988) corrected for wavenumbers greater than 200  $\text{cm}^{-1}$  by a factor linearly increasing to 1.75 for wavenumbers greater than 300  $\text{cm}^{-1}$  and is constant for larger wavenumbers (see text). This correction improves the fit to the IRIS data. Successive curves are offset in the vertical by 5K. The third set of curves is for the nominal cloud case listed in Table I and the fourth set of curves are for the nominal cloud case with the  $\text{CH}_4\text{-N}_2$  correction. The presence of the cloud also improves the fit to the data. The uppermost curves are a comparison of the IRIS brightness temperatures with the model predictions for the optimized cloud model (Table II, case 5a; Table III).



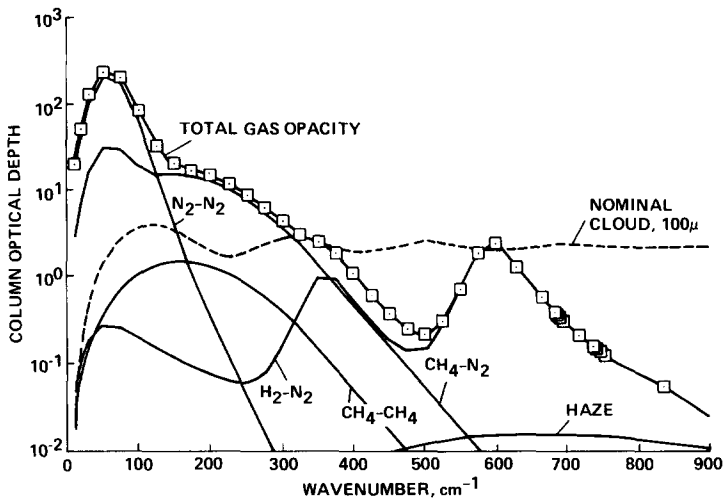


FIG. 8. Total thermal infrared column opacity for baseline no-cloud case, as defined in the text and listed in Table I, using the Voyager egress temperature profile. Absorption due to pure  $N_2$  and  $CH_4$  and by  $N_2$ - $CH_4$  and  $N_2$ - $H_2$  mixtures are computed based on the method of Courtin (1988). The sum of all the gaseous absorption is also plotted with markers at each of the wavenumber points used in computations in the model. Also shown is the extinction due to haze particles and the dashed line shows the extinction due to the nominal  $CH_4$  cloud composed of particles of  $100\text{-}\mu\text{m}$  radius with an optical depth of 2 at  $200\text{ cm}^{-1}$ .

an emission angle of  $60^\circ$ , which only approximates the IRIS observations which were at  $52.7^\circ$ . Nonetheless, our total haze adjustment required to match the IRIS data ( $C_0X_i = 0.35 \times 0.5 \approx 0.2$ ) agrees with the total reduction suggested in the more detailed study by Toon *et al.* of 0.25, as shown in their Fig. 8, curve 3. The advantage of our approach is that we are able to separate the reduction in haze emission due to haze optical properties from that due to haze production rates. Figure 7 also shows the fit for several other cases that are discussed below. Although the model calculations are systematically lower than the data in the  $500\text{--}600\text{ cm}^{-1}$  region, there is an overall agreement that suggests that our choice of model parameters is indeed constrained by the data set.

In Fig. 8 the thermal infrared column opacity for the baseline no-cloud case and the nominal cloud is shown. The sum of all the gaseous absorption is also plotted with markers at each of the wavenumber points used in the model. Also shown is the ex-

tingtion due to haze particles and the dashed line shows the extinction (chiefly scattering) due to the nominal  $CH_4$  cloud composed of particles of  $100\text{-}\mu\text{m}$  radius with an optical depth of 2 at  $200\text{ cm}^{-1}$ .

Figure 9 shows the column optical depths for the haze and for Rayleigh scattering in the visible for the baseline no-cloud case listed in Table I. Also shown is the optical depth of the nominal cloud. Markers on the Rayleigh scattering curve indicate the mid-points of the spectral intervals used in the model to compute the solar energy deposition.

The procedure outlined above for fitting the model parameters to the observational data sets has proven to be quite satisfactory. We have developed the model in such a way as to minimize the number of free parameters. In addition, we have used laboratory data sets to set the optical constants of the materials in the atmosphere. When required we have scaled the laboratory results by a single factor and were still able to obtain good fits. Thus, the baseline no-

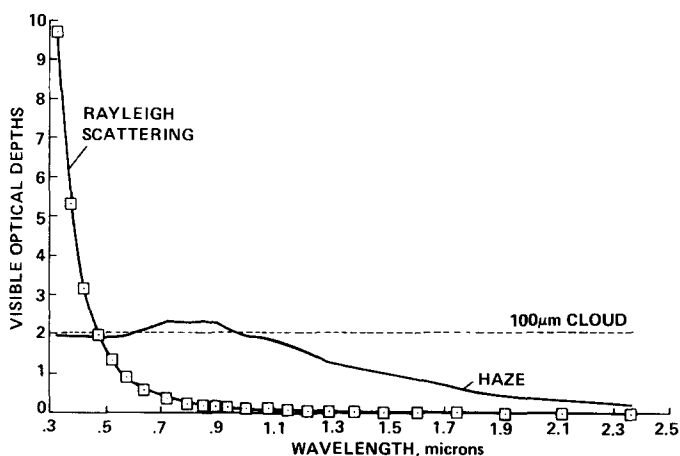


FIG. 9. Column optical depths in the visible for the haze and for Rayleigh scattering for the baseline no-cloud case listed in Table I. Also shown, as a dashed line, is the optical depth of the nominal cloud. Markers on the Rayleigh scattering curve indicate the midpoints of the spectral intervals used in the model to compute the solar energy deposition.

cloud model contains only nine physical quantities that must be specified to completely and uniquely determine the atmospheric structure. Since we have not used the temperature profile determined by Voyager as one of the observational constraints (although we have used that temperature profile to define the atmosphere for the purposes of fitting to the IRIS data), we can perform an independent calculation of temperature.

*Nominal cloud case.* For the baseline no-cloud case, the best-fit set of parameters listed in Table I was obtained assuming that there was no condensation cloud near the temperature minimum. In fact both ethane and methane have regions of saturation in the atmosphere. Ethane saturation extends from 55 to 35 km while methane saturation extends from about 5 to 30 km. The ethane condenses above the temperature minimum and methane below due to the fact that the source for ethane is above and that for methane is below this minimum. Ethane may also have a source at the surface (Lunine *et al.* 1983).

Since we have included a condensate cloud without an associated microphysical

model, the presence of a cloud introduces several new free parameters into the model. These are the particle size and optical depth, both as functions of altitude. The presence of a cloud in the atmosphere slightly alters the fit to the observational data sets. Toon *et al.* (1988) have shown that the IRIS data can be used to place constraints on the particle sizes and optical depths of any condensation clouds. We use their best-fit cloud case (particle radius =  $100\text{ }\mu\text{m}$ , optical depth at  $200\text{ cm}^{-1} = 2$ , with opacity distributed proportional to the methane gas amount within the saturated layers) as the nominal cloud case. The fit of the IRIS data for this cloud is shown as the third curve from the bottom in Fig. 7, and it can be seen that the fit is somewhat improved over the baseline no-cloud case (bottom curve in Fig. 7). For the geometric albedo, the effect of such a cloud is to increase the albedo, most significantly in the continuum points at  $0.827\text{ }\mu\text{m}$ ,  $0.935\text{ }\mu\text{m}$ , and longer. This is expected since at shorter wavelengths Rayleigh scattering and absorption by the haze at altitudes well above the cloud prevent the cloud from having any effect on the reflected light.

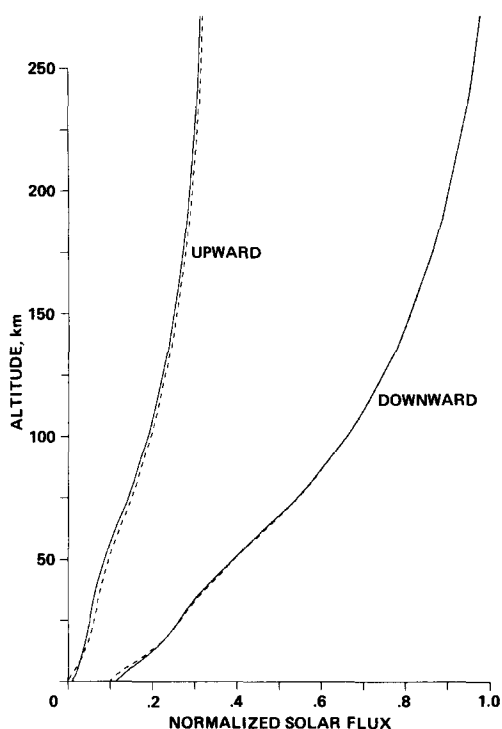


FIG. 10. Altitude profile of the downwelling solar flux (right-hand set of curves) and the upwelling solar flux (leftmost set of curves). The solid lines are for the baseline no-cloud case and the dashed lines are for the nominal cloud case listed in Table I.

While the extinction of the small Rayleigh and haze particles falls off steeply with increasing wavelength, the comparatively huge cloud particles are still efficient scatterers in the long wavelength visible light. Without a cloud present, solar energy at these wavelengths, outside of the methane bands, would reach the ground and be reflected. The presence of the cloud introduces a reflective layer above the ground offsetting a low surface albedo. For the nominal cloud case to produce a fit with the geometric albedo data that is as close as was determined with the baseline no-cloud case a slight adjustment of the parameters,  $X_v$ ,  $A_v$ , and  $X_i$ , is required. As listed in Table I, and as expected from the discussion of the effects of the cloud, we find that setting  $A_v$  to zero, while retaining the pre-

vious values of  $X_v$  and  $X_i$ , is the simplest adjustment that restores the original fit. This value of  $A_v$  also works well for the cloud of particles  $60 \mu\text{m}$  in radius, which is considered below.

## RESULTS AND DISCUSSION

When the temperature of the model is held fixed at the profile based on the Voyager egress data, as described before, several quantities related to the radiation balance that are of interest can be computed. The upward and downward fluxes of solar energy are shown in Fig. 10 both for the nominal cloud free case and for the nominal cloud case. In both cases the downwelling flux exceeds the upwelling flux but only by a factor of 2 to 3. The presence of the condensate cloud perturbs the downwelling flux near and below the cloud height only. The upwelling flux is slightly increased everywhere above the cloud height and slightly decreased below it. Overall the effect of the cloud on the visible radiation field is small. This is further illustrated in Fig. 11 which shows the spectral distribution of energy that reaches the surface. The results for the nominal cloud model (dotted line) are very close to those for the baseline no-cloud model (solid line).

Figure 12 shows the altitude in the baseline no-cloud model at which extinction op-

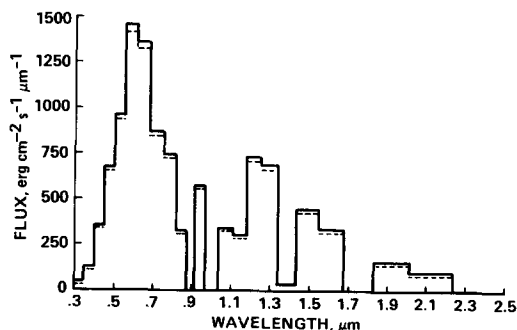


FIG. 11. Solar energy absorbed by the surface in the baseline no-cloud case (solid line) and for the nominal cloud case (dashed line) for each spectral interval in the model. The energy absorbed is determined by the area under the curve.

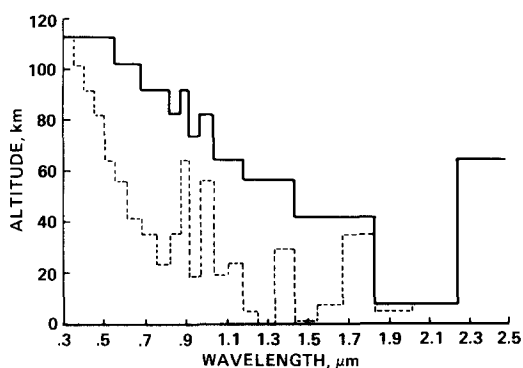


FIG. 12. The altitude at which the normal extinction optical depth reaches a value of unity, plotted as a solid line, for each spectral interval. Also shown, as a dashed line, is the altitude at which the downwelling visible flux is  $e^{-1}$  of the incoming solar flux at that wavelength. Results are for the no-cloud baseline model as listed in Table I.

tical depth unity is reached for each spectral interval. Also shown, as the dotted line, is the altitude at which the downwelling solar flux is  $e^{-1}$  of the incoming solar flux at that wavelength. The two lines are not the same since scattering effects cause the downwelling solar flux to deviate from Beer's law. There are two interesting features of this result. First in the short wavelengths ( $<0.7 \mu\text{m}$ ) the direct solar beam is attenuated at relatively high altitude but a fraction of the flux is scattered down toward the surface. At longer wavelengths ( $>1 \mu\text{m}$ ) most of the incoming radiation reaches the surface.

Although proportionally more of the longer wavelength radiation reaches the surface, the shorter wavelength radiation is more effective in heating the surface—as seen Fig. 11. The total fraction of sunlight incident on Titan that is absorbed by the surface in the baseline no-cloud case is 10.3%. For the nominal cloud case the corresponding value is 9.9%. Figures 11 and 12 show that the stratosphere is heated primarily by the short wavelength visible light and the surface is heated more or less equally by wavelengths below  $0.7 \mu\text{m}$  and above  $1 \mu\text{m}$ .

The model provides a means for the direct computation of the Bond albedo of Titan, consistent with the geometric albedo. For our baseline no-cloud model we obtain a Bond albedo of 32% with less than 1% increase for the nominal cloud case. Our results imply a value of  $T_{\text{eff}}$  of  $81.8^\circ\text{K}$ . Considering the fairly broad spectral intervals used in the calculation, our estimate compares well with the results of Neff *et al.* (1985) of  $83 \pm 2^\circ\text{K}$  and that of Tomasko and Smith (1982) of  $84 \pm 2^\circ\text{K}$ .

In Figure 13 the net radiative flux at the surface in the thermal infrared is plotted for each spectral interval for the baseline no-cloud case. There are two main features in Fig. 13: cooling of the surface below  $600 \text{ cm}^{-1}$  and small heating of the surface by the stratospheric emissions between  $700$  and  $900 \text{ cm}^{-1}$ . The low opacity of the atmosphere in the region from  $400$  to  $600 \text{ cm}^{-1}$  makes this the “window” region of Titan. Since the peak of the Planck function ( $B_\lambda d\lambda$ ) at  $94^\circ\text{K}$  is at  $\sim 330 \text{ cm}^{-1}$  this window occurs at a spectral location containing significant amounts of radiation and so it controls the greenhouse effect of Titan's atmosphere. If the surface were to warm to higher temperatures the radiation peak

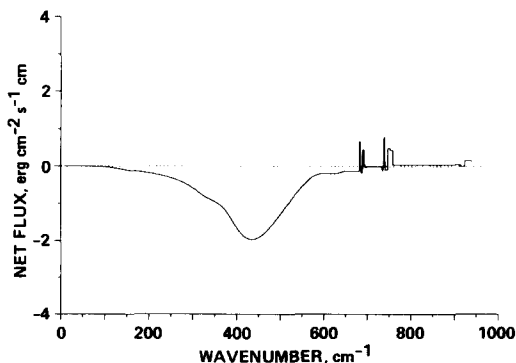


FIG. 13. Net thermal infrared energy balance at the surface in the baseline no-cloud case. The net energy balance is determined by the area under the curve. The spikes near  $700\text{--}800 \text{ cm}^{-1}$  are due to heating of the surface by stratospheric gases. The total area under the curve is  $-379 \text{ erg cm}^{-2} \text{ sec}^{-1}$ .

would shift even more into the window region where the surface could radiate even more efficiently to space.

Another effect seen in Fig. 13 is the heating of the surface due to radiation emitted by stratospheric gases. The Titan stratosphere is much warmer than the surface but is not able to effectively heat the surface at wavenumbers at which it emits radiation due to the low opacity of its gases and haze particles at these wavelengths (at 170°K the maximum of the Planck function is at  $600\text{ cm}^{-1}$ ). However, in portions of the  $700\text{--}900\text{ cm}^{-1}$  region, stratospheric gases are optically thick and tropospheric gases are optically thin and so the former can heat the surface. The flux received by the ground due to the stratospheric gaseous emissions of  $\sim 19\text{ erg cm}^{-2}\text{ sec}^{-1}$  is  $\sim 5\%$  of the net thermal infrared radiation lost by the surface ( $-379\text{ erg cm}^{-2}\text{ sec}^{-1}$ ) as shown in Fig. 13. Because of the ease with which radiation can leave the surface through the infrared window region the change in surface temperature per unit change in flux is quite low. By doing incremental perturbation studies we have calculated it to be  $0.02^\circ\text{K erg}^{-1}\text{ cm}^2\text{ sec}$ . This would imply that the flux contributed to the surface due to the stratospheric gaseous emissions results in only a  $\sim 0.5^\circ\text{K}$  increase in surface temperature. A further implication of this result is that a significant increase in the solar energy reaching the surface will have only a modest effect on the surface temperature, unless the infrared opacity is also changed. For example, if the solar energy deposition is increased from 10 to 15% of the incident flux (an increase of  $185\text{ erg cm}^{-2}\text{ sec}^{-1}$ ), then, all other things remaining constant, the surface temperature will increase by only  $4^\circ\text{K}$ .

A measure of the radiative equilibrium of the baseline no-cloud model and the nominal cloud model is shown in Fig. 14. This is a plot of the net radiative flux (combined visible and thermal infrared fluxes) divided by the sum of the absolute magnitudes of visible and thermal infrared net fluxes,  $F/$

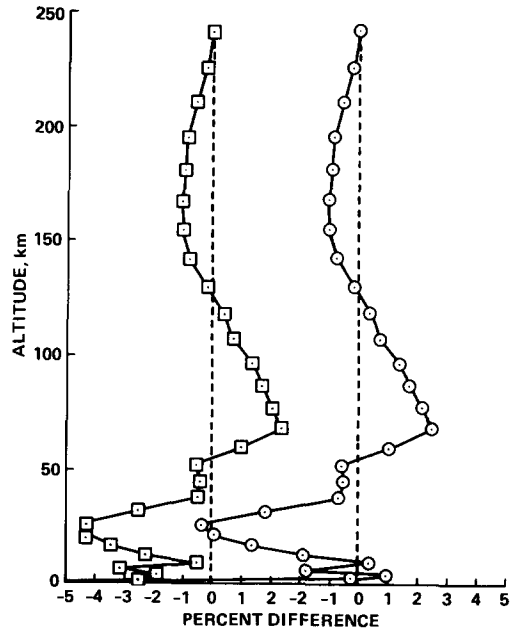


FIG. 14. The net flux (both visible and thermal infrared summed) divided by the sum of the absolute magnitudes of visible and thermal infrared flux. Positive values indicate a warming and negative values a cooling. If the model was in perfect thermal balance this term would be zero everywhere except near the surface where the radiative balance would be positive since some of the solar energy deposited in this region would be carried by convection. Results are shown for the baseline no-cloud case (left curve) and for the nominal cloud case (right curve) as described in Table I.

$(|F_v| + |F_{IR}|)$ . Positive values mean that the atmosphere is warming and negative values mean that the atmosphere is cooling. If the models were in perfect thermal balance this term would be zero everywhere except near the surface where the radiative balance would be negative since some of the solar energy deposited at the surface is carried upward by convection.

Until this point all the results presented have been obtained using the model in a diagnostic sense. That is, the temperature profile has been fixed to the observed value and the thermal balance in the atmosphere has been computed. We have also performed calculations in which we allow the temperature profile of the atmosphere to change in order to achieve thermal radiative

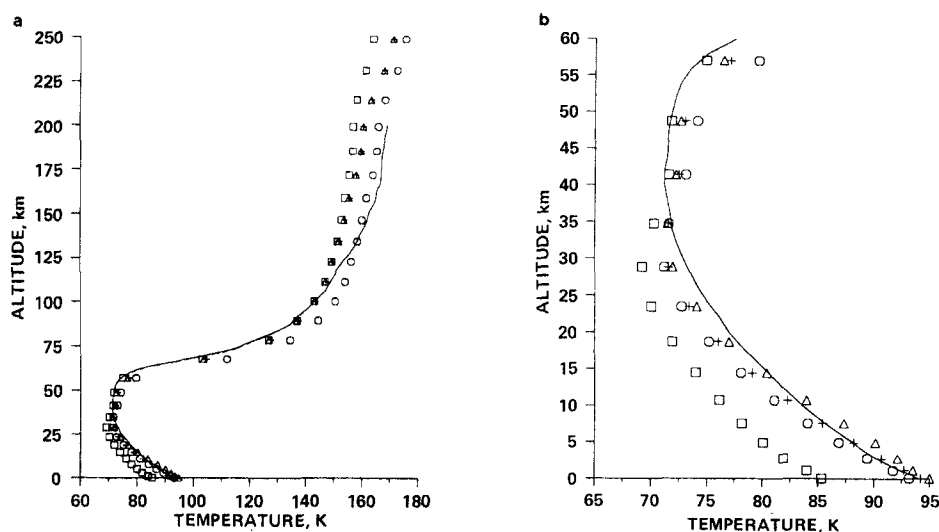


FIG. 15. Radiative equilibrium temperature profile of the atmosphere for the baseline no-cloud case (see Table I) is shown as squares with the Voyager egress data of Lindal *et al.* (1983) shown as a solid line. The model results in this case are computed with all of the parameters chosen by comparison of model predictions to observational data sets *other* than the temperature profile. Thus no model parameters have been adjusted to enhance the fit shown in this figure. Also shown are the various optimized cases. Radiative equilibrium temperature profile of the atmosphere for the optimized no-cloud case (see Table II, case 3g; Table III) is shown as circles. The radiative equilibrium temperature profile of the atmosphere for the optimized cloud case (see Table II, case 5a; Table III) is shown as triangles. The temperature profile with the cloud removed (Table II, case 3h) is virtually identical to the model results shown and is shown as pluses.

tive-convective equilibrium. The resulting temperature profile for the baseline no-cloud case is shown in Fig. 15. The results are tabulated in Table II as case 3. The temperature profile for the nominal cloud case would be virtually indistinguishable at the scale of the plot (Table II, case 4).

Although the fractional net radiative flux of the baseline no-cloud case is everywhere less than  $\sim 5\%$ , the converged temperature profile is clearly cooler than the Lindal *et al.* (1983) values adjusted for the composition of the atmosphere (Table II, cases 1a-1c). This is also true for the nominal cloud model. In particular the models are cooler in the stratosphere by about  $10^\circ\text{K}$  and cooler in the troposphere by about  $5\text{--}10^\circ\text{K}$ . We have performed a series of sensitivity studies to determine if changes in any single parameter would result in smaller differences.

We note that the comparison of a globally

averaged calculation with a measured profile at a single point (such as the Lindal *et al.* results) must be viewed with caution. In addition dynamical effects, not included in this one-dimensional study, may be significant.

The cool stratosphere is primarily due to neglect of solar radiation below  $0.3\ \mu\text{m}$ . We have corrected this by scaling the solar flux in the first two wavelengths by a factor of 2.5. An alternate way of altering the stratospheric temperature without affecting the various observational constraints on the geometric albedo or the IRIS emission spectrum would be to alter the concentration of those trace gases that are radiatively active in the thermal infrared. If the stratospheric mixing ratios of  $\text{C}_2\text{H}_2$  and  $\text{C}_2\text{H}_6$  are reduced by a factor of approximately 5, then the computed stratospheric temperatures are in much improved agreement with the Lindal *et al.* (1983) values. An adjust-

TABLE II  
TEMPERATURE RESULTS FOR SEVERAL CASES

Case	Surface $T^a$	Tropopause $T$
1. Lindal <i>et al.</i> (1983)	94.0	71.2
1a. $\text{RH}_{\text{CH}_4} = 60\%$ , $f_{\text{H}_2} = 0.3\%$	93.3	70.6
1b. $\text{RH}_{\text{CH}_4} = 30\%$ , $f_{\text{H}_2} = 0.3\%$	93.0	70.6
1c. $\text{RH}_{\text{CH}_4} = 60\%$ , $f_{\text{H}_2} = 0.6\%$	92.8	70.4
1d. $\text{RH}_{\text{CH}_4} = 60\%$ , $f_{\text{H}_2} = 0.3\%$ , $\text{Ar} = 10\%$	96.6	73.2
2. No adjust, $C_o = X_v = X_i = 1$	78.8(86.0)	66.77
3. Baseline no-cloud (see Table I)	85.3(90.2)	70.2
3a. $\text{RH}_{\text{CH}_4} = 100\%$	85.3(90.4)	70.3
3b. $f_{\text{H}_2} = 0.6\%$	88.1(91.5)	70.2
3c. $\text{CH}_4\text{-N}_2$ adjust	87.3(91.9)	70.1
3d. $C_o = 0.2 (\times 3.5 \times 10^{-14} \text{ g cm}^{-2} \text{ sec}^{-1})$	90.2(92.7)	71.2
3e. $X_v = 1.0$	85.7(90.5)	70.1
3f. $\langle \theta \rangle_h \times 1.1$	87.1(91.0)	70.7
3g. Optimized (see Table III)	93.2(94.2)	71.6
3h. Optimized (case 5a without cloud)	94.2(94.5)	71.5
4. Nominal 100- $\mu\text{m}$ cloud (see Table I)	86.8(91.3)	70.3
4a. $n_i = 10^{-4}$	86.1(89.5)	69.8
4b. $n_i = 10^{-3}$	83.4(85.9)	69.8
4c. $\text{CH}_4\text{-N}_2$ adjust	88.5(92.8)	70.1
4d. $\text{CH}_4\text{-N}_2$ adjust, $n_i = 10^{-4}$	88.5(94.0)	70.1
4e. $\tau_c = 5$	88.3(91.9)	70.2
4f. $\tau_c = 10$	89.8(92.6)	70.1
5. 60- $\mu\text{m}$ cloud	86.3(91.3)	70.2
5a. Optimized (see Table III)	95.0(94.4)	71.5

<sup>a</sup> Numbers in parentheses refer to the surface temperature computed with the methane profile held fixed based upon Voyager data, i.e., not iterated with the temperature calculations.

able parameter in the model that would also affect the stratospheric temperature is the haze absorption,  $X_i$ . However, changes in this parameter affect the fit to the IRIS data.

Table II lists the effects on the surface temperature and the tropopause temperature for a series of changes in the model. The first set of entries entry in Table II is just the values from the Voyager egress profile from Lindal *et al.* (1983). Case 1 is the Lindal results for a pure  $\text{N}_2$  atmosphere. Cases 1a–1d are the results of modifying the Lindal *et al.* profile for the atmospheric compositions listed. In this table the results are listed to 0.1°K. This is much better than the accuracy of the procedures used, but is valid when considering differ-

ences between cases. For the model calculations the surface temperature and tropospheric temperature minimum are listed. In addition the surface temperature that would be obtained if the model was allowed to come to convergence without iterating on the methane composition is listed. In this mode the feedback between the surface temperature and the methane concentration is artificially suppressed and the methane profile is held fixed to the value determined by the Voyager egress data as described in the initial sections of the model description. As will be seen, the inclusion of this feedback considerably amplifies any deviations from the Voyager results.

To illustrate the importance of the observational data sets in defining the model we

have computed the temperature profile for the case in which three of the model parameters are set to the values that one would use based only on previous models of the haze production and laboratory analogs (Chang *et al.* 1979, Yung *et al.* 1984, Khare *et al.* 1984). The results, case 2, differs significantly from the baseline case (3) and is in very poor agreement with the Lindal *et al.* (1983) results.

To warm up the troposphere we have tried increasing the surface relative humidity of methane (case 3a). This has very little effect on the model even though methane is one of the key, albeit modest, absorbers in the window region of the thermal infrared. The reason for this is that increasing the surface relative humidity only increases the mixing ratio of methane in the lower layers of the atmosphere, since above a few kilometers methane reaches its saturated value even in the baseline model. One consequence of this is that the atmospheric temperature profile is fairly independent of the presence or composition of an ethane rich ocean that may suppress the relative humidity of methane at the surface.

Since  $H_2$  is uniformly mixed in the model, and also has absorption in the window region, changes in the hydrogen mixing ratio can potentially have a much more pronounced effect than changes in the relative humidity of methane. However, changes in the hydrogen mixing ratio must be offset by changes in the haze thermal infrared absorption factor or the fit with the IRIS data will deteriorate (Thompson and Sagan 1984, Toon *et al.* 1988). Furthermore, Toon *et al.* (1988) have shown that this balance can match the IRIS data only for values of the hydrogen mixing ratio of 0.6% or less. In Table II, case 3b, we have listed the effect of such an increase on the baseline model.

The pressure induced opacity coefficient for  $CH_4-N_2$  determined by the method of Courtin (1988) is slightly below the laboratory data for wavenumbers above  $200\text{ cm}^{-1}$  at the lowest temperature for which data

are available ( $126^\circ\text{K}$ ). Increasing his results by a factor that is unity at and below  $200\text{ cm}^{-1}$ , increases linearly to 1.75 at  $300\text{ cm}^{-1}$ , and remains constant at that value at higher wavenumbers forces the calculations to agree with the laboratory data. It should be emphasized that this is not an ad hoc correction and in fact merely forces agreement with the data. This correction effectively enhances the absorption due to methane. Toon *et al.* (1988) have found that such a correction improves the fit of the Titan model atmospheric emission spectra to the IRIS data. This is shown in Fig. 7, where the second from the bottom and the top curves are the emission spectra computed for the baseline no-cloud case and the nominal cloud case, respectively, with this adjustment to the  $CH_4-N_2$  pressure-induced absorption. The effect on the troposphere temperature is shown in Table II, case 3c. Since the absorption varies as the square of the pressure its effects are confined to the troposphere. Toon *et al.* (1988) have also included an additional 25% correction to the  $CH_4-N_2$  absorption coefficient above that indicated by the data—we do not use this correction here.

For all the corrections considered so far the troposphere becomes warmer since the same amount of visible light reaches the surface but the infrared opacity is increased. As seen in Table II, cases 3a–3c, no single correction that deals with the infrared opacity and the infrared active gases is sufficient to reach the desired temperatures. We have to consider therefore corrections to the model that will allow more solar energy to reach the troposphere and the surface. We have considered the effects of a lower production rate of haze material ( $C_0 = 0.2$  in case 3d). This results in smaller particles, a decrease in the altitude of optical depth unity, and a reduction in total optical depth of the haze. This significantly improves the fit of the temperature model to the Voyager egress results. However, the value of  $C_0$  is strongly constrained by the geometric albedo, particularly in the



methane bands at 0.620 and 0.888  $\mu\text{m}$ , as shown in Fig. 6, and it is difficult to compensate for the reduction in the albedo of these points by corresponding changes in the other model parameters. In fact, due to the resulting reduction in geometric albedo at 0.620 and 0.888  $\mu\text{m}$  we are unable to lower the value of  $C_0$  below 0.3.

Altering the haze optical properties can also influence the amount of light that reaches the surface. This is shown (case 3e) for haze optical constants set directly to the results of Khare *et al.* (1984).

Another direct way of increasing the flux reaching the troposphere is to alter the scattering properties of the haze particles. There is significant evidence that the haze particles are nonspherical in nature (Tomasko and Smith 1982, Rages *et al.* 1983) and it is possible that the spherical Mie computations used in the model do not correctly determine the scattering asymmetry factor. If the scattering asymmetry factor of the haze particles is everywhere increased by 10%, the surface and troposphere warm as shown in Table II, case 3f.

Adding the methane condensation cloud to the model and changing the surface albedo to zero to continue to match the geometric albedo, as discussed in conjunction with Table I, do not produce a significant warming in the troposphere, as seen in Table II, case 4. Correcting the  $\text{CH}_4\text{-N}_2$  infrared absorption (case 4c) or introducing a small component of absorption in the visible to the methane cloud by increasing the imaginary index of refraction to  $10^{-4}$  (cases 4a and 4b) slightly improves the overall tropospheric temperature profile. Effectively the increased absorption in the cloud heats the region of the atmosphere from 5–30 km greatly improving the agreement with the data in that region. However, since no other parameters in the model have been changed the surface is receiving less radiation and is slightly cooler. Coupling a slightly absorbing cloud with increased opacity, such as the  $\text{CH}_4\text{-N}_2$  correction, could improve both aspects of the model

temperatures, as shown in case 4d. Increasing the cloud index of refraction to  $10^{-3}$  (case 4b) produces a pronounced effect on the surface temperature. The absorbing cloud warms the troposphere in its vicinity but severely attenuates the solar flux reaching the ground, causing unrealistically low surface temperatures. The increased visible absorption, which could represent the effects of haze material or other dark organic substances held within the cloud particles, does not affect the thermal emission of the cloud and hence does not alter the fit to the IRIS data.

When clouds are present the radiative balance of the atmosphere is greatly affected by the size of the cloud particles. The presence of a cloud affects both the incoming solar radiation and the outgoing thermal infrared radiation. Figure 16 shows the solar energy absorbed (solid lines with markers) by the surface and the net thermal infrared energy loss (dashed lines with markers) for varying cloud particle sizes. Also shown, for comparison, are the corresponding values for the baseline no-cloud case. The solar energy absorbed is the fraction of the total sunlight incident on Titan that is absorbed at the surface. The net thermal infrared energy loss is the radiation emitted from Titan's surface less the radiation that the surface receives from the sky. In order for the surface to be in radiative equilibrium the solar energy deposition and the thermal infrared losses must be near balance. Even though the Voyager results indicated that Titan's atmosphere seems to be in radiative balance, there will be some convection energy carried from the surface. Therefore, for radiative-convective balance the solar energy absorbed must be larger than the net thermal infrared energy emitted.

For all cases of different cloud particle sizes the cloud opacity is held fixed at 2 optical depths at 200  $\text{cm}^{-1}$  and the thermal structure is held fixed at the egress profile. The surface albedo for all the cloud cases is set to zero, consistent with the nominal

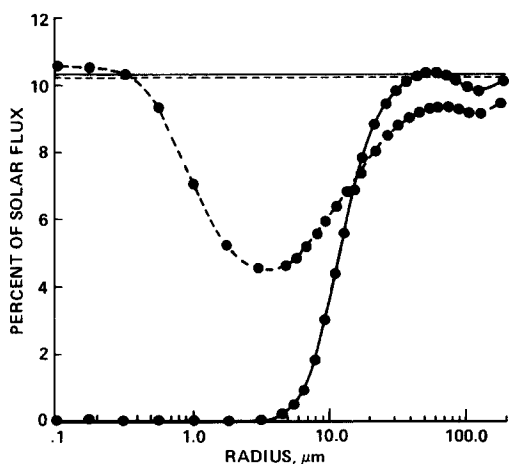


FIG. 16. The solar energy absorbed by the surface and the thermal infrared energy loss for varying cloud particle sizes. The opacity in each case is held fixed at 2 at  $200\text{ cm}^{-1}$  and the temperature structure is held fixed at the Voyager temperature profile. The solid line is the solar energy absorbed at the surface; the straight solid line shows the result for the baseline no-cloud case. The dashed line refers to the net thermal infrared radiation lost from the surface and the straight dashed line refers to the baseline no-cloud case. For clouds of sub  $10\text{ }\mu\text{m}$  particles essentially no solar energy reaches the surface to balance the thermal infrared losses. The slight increase in solar absorption at  $\sim 60\text{ }\mu\text{m}$  compared to the no-cloud case is due to the fact that the surface albedo is zero in the cloud case and 0.1 in the no-cloud case (see Table I).

cloud results in Table I. For very small particles the optical depth in the visible is enormous and even for virtually pure scatterers essentially no solar radiation reaches the ground. Such submicrometer clouds are consistent with the IRIS emission spectra (Thompson and Sagan 1984, Toon *et al.* 1988) as are much larger cloud particles ( $r_c > 50\text{ }\mu\text{m}$ , Toon *et al.* 1988). The presence of a submicrometer cloud also helps reduce the net thermal infrared cooling by the surface which reaches a minimum of about 4.5% of the solar flux. It is possible that micrometer-sized and submicrometer-sized methane condensation clouds exist in Titan's atmosphere. If they do they must be patchy, allowing some solar energy through. Since the cloud-free atmosphere on Titan seems to be close to radiative bal-

ance, that is, the absorbed solar radiation appears to closely balance the net thermal infrared losses, any coverage of small particle clouds would significantly alter the thermal structure. Based upon the sensitivity of the surface temperature to changes in flux we estimate that a  $5^\circ\text{K}$  decrement in surface temperature would result from an areal fraction of small particle methane clouds of 60%. A model calculation in which we "removed" 50% of the solar flux in the troposphere resulted in a  $5.3^\circ\text{K}$  temperature drop in the baseline no-cloud model, confirming the magnitude of our estimate.

As the methane cloud particles become larger their effect on the surface heat balance reverses. Particles larger than a few tens of micrometers have a net greenhouse effect since they essentially do not lower the solar flux reaching the surface but do decrease the net thermal infrared losses from the surface. This is due to the fact that the clouds are pure scatterers in the visible but are scattering absorbers in the infrared. The effect of particle size on the solar and thermal infrared radiation balance of the surface as shown in Fig. 16 exemplifies the scattering greenhouse effect discussed by Samuelson (1967) for Venus and by McKay and Pollack (1984) for Titan. Our results for the crossover value for the methane cloud particles ( $\sim 20\text{ }\mu\text{m}$ ) agree well with a simple uniform gray scattering model which would predict that methane cloud particles larger than  $30\text{ }\mu\text{m}$  will produce a scattering greenhouse effect. From the plot it is clear that the optimal particle size for surface warming is  $\sim 60\text{ }\mu\text{m}$ . However, as seen in Table II (case 5) the effect of clouds (with both 60- and  $100\text{-}\mu\text{m}$  size particles) is only a degree or so. This is due to the constraint that the cloud opacity be 2 at  $200\text{ cm}^{-1}$ , to ensure a good fit to the IRIS emission data. This implies an optical depth in the visible 1 and 2 for the 60- and  $100\text{-}\mu\text{m}$  clouds, respectively. If the cloud optical depth is increased to 5 or 10 the surface temperature does increase as seen in Table II, cases 4e and 4f.

TABLE III  
MODEL ADJUSTABLE PARAMETER SETTINGS FOR  
OPTIMIZED CASES

Variable	Values for optimized case	
	No-cloud	Cloud
Charging radius, $r_c$	0.09 $\mu\text{m}$	0.09 $\mu\text{m}$
Pressure of haze production, $P_0$	$10^{-14}$ mb	$10^{-14}$ mb
Haze production rate, $C_0$	0.30 <sup>a</sup>	0.35 <sup>a</sup>
Haze visible absorption factor, $X_v$	1.2	1.1
Haze infrared absorption factor, $X_i$	0.5	0.7
Surface relative humidity, $\text{RH}_{\text{CH}_4}$	60%	60%
H <sub>2</sub> mixing ratio, $f_{\text{H}_2}$	0.3%	0.4%
Visible surface reflectance, $A_v$	0.2	0.2
Infrared surface reflectance, $A_{\text{ir}}$	0	0
Methane cloud particle radius, $r_{\text{cl}}$	—	60 $\mu\text{m}$
Opacity of cloud at 200 $\text{cm}^{-1}$ , $\tau_{\text{cl}}$	—	2
Other adjustments		
Cloud imaginary index, $n_i$	—	$10^{-4}$
Haze asymmetry factor, $\langle\theta\rangle_h$ , scaling	1.1	1.1
Solar UV increased by	2.5	2.5
CH <sub>4</sub> -N <sub>2</sub> adjustment factor	1 : $\nu < 200 \text{ cm}^{-1}$ ; 1.75 : $\nu > 300 \text{ cm}^{-1}$ ; linear between	

<sup>a</sup> In units of  $3.5 \times 10^{-14} \text{ g cm}^{-2} \text{ sec}^{-1}$ .

#### OPTIMIZED CASES

In this subsection we attempt to optimize the fit of the model temperatures to the Voyager egress results of Lindal *et al.* (1983), while at the same time remaining as consistent as possible with the observational data sets used before for the selection of the model adjustable parameters. As we show below, we have been able to do this fairly well for both a no-cloud case and for a 60- $\mu\text{m}$  cloud case. The fits we derive are not unique but serve to illustrate the range of variation that is required to bring the model into agreement with the observations.

In order to optimize the fit for the no-cloud case we included the correction to the CH<sub>4</sub>-N<sub>2</sub> pressure-induced absorption. This is the only correction in the thermal infrared (for this case) and, as shown before in Fig. 6, this actually results in an improved fit to the IRIS spectra over the base-

line no-cloud case. In the visible portion of the spectrum we lowered  $C_0$ , the haze production rate, while compensating for the changes in the geometric albedo by raising the surface albedo and lowering the imaginary index of refraction of the haze particles. We were able to obtain the combination of parameters listed in Table III. This produces a fit to the geometric albedo shown in Fig. 5. In order to allow more solar flux to reach the tropopause and the surface we have increased the scattering asymmetry factor of the haze particles everywhere by 10%. In addition we increased the solar flux in the first two spectral intervals by a factor of 2.5 to warm the stratosphere. The distribution of solar energy in the baseline model neglects extreme UV photons which could be a heating source in the stratosphere. Increasing our UV spectral intervals by 2.5 is meant to account for these terms. The resulting temperature profile is shown in Fig. 15 and agrees fairly well

with the Lindal *et al.* (1983) results. The fraction of the total solar energy absorbed by the surface in this case is 10.2%. The surface and tropopause temperatures are listed in Table II, case 3g.

Even in the optimized no-cloud case (shown in Fig. 15) the temperatures in the region of methane saturation are a bit cool. This suggests that the inclusion of a cloud followed by reoptimization might improve the fit. We have therefore included a cloud of 60- $\mu\text{m}$  particles with slightly absorbing particles ( $n_i = 10^{-4}$ ). In addition we have increased the concentration of  $\text{H}_2$  to 0.4% (still less than the 0.6% limit discussed above). Both of these changes will increase the temperatures in the upper troposphere. In addition we have set the haze production rate to 0.35 and the haze visible absorption factor to 1.1, the asymmetry factor has been increased by 10%, and the  $\text{CH}_4\text{-N}_2$  pressure-induced absorption has been adjusted as described above. All of these changes tend to warm the surface and atmosphere. To remain consistent with the geometric albedo and IRIS emission data sets requires corrections to several other model parameters as listed in Table III, including the surface albedo which is set to 0.2. Most significantly the haze infrared absorption factor is increased from 0.5 to 0.7 in order to compensate for the increase in the hydrogen mixing ratio. This increases the IR cooling by the haze and tends to lower the stratosphere temperatures a bit. The new fits to the geometric albedo and IRIS emission data sets are shown in Figs. 5 and 7. The resulting temperature profile is shown in Fig. 15. The fit in the region of methane saturation is slightly improved over the optimized no-cloud case. The fraction of the total solar energy absorbed by the surface in this case is 7.7% but this reduction in solar heating is offset by the increase in thermal infrared opacity—part of which is due to the cloud (see Figs. 8 and 16). The surface and tropopause temperatures are listed in Table II, case 5a.

A slightly different approach to optimiz-

ing the temperature results was followed when we considered the no-cloud case as compared with the cloud case. In particular the optimized baseline no-cloud case (Table II, case 3g, Table III, and Fig. 15) was derived primarily by changing the haze production rate and visible properties while leaving the thermal infrared properties as they were. In the cloud optimization (Table II, case 5a, Table III, Fig. 15) the converse approach was followed. It is therefore useful to consider the case in which the cloud is simply removed from the optimal cloud case leaving all of the other parameters alone. This result is shown as the plus marks in Fig. 15. The values are not very different from the temperature that resulted from the inclusion of the cloud. However in this case the fraction of solar energy reaching the surface is 9.6%, which is larger than the corresponding value when the cloud was included. This case is listed in Table II as case 3h. Again this illustrates that any methane condensation cloud, if present on Titan, plays a minor role in the temperature structure. Ethane clouds above the cold trap gave much the same results as the methane clouds discussed above.

## CONCLUSIONS

Our approach to modeling of Titan's atmosphere has been based on utilizing all the available observational data sets to define a radiative-convective equilibrium model. This approach has proven to be successful and illustrates the importance of developing self-consistent models of Titan's atmosphere that agree with the observational constraints, including spectral observation from the ultraviolet to the thermal infrared. We have been able to construct models that closely match the observed temperature profile of Titan's atmosphere while at the same time being consistent with the observational constraints on the models.

Based upon our models of Titan's thermal structure we can draw several conclusions. We feel that the thermal structure of Titan's atmosphere can be fairly well fit

without invoking methane or ethane condensation clouds. This does not argue against the presence of such condensation clouds but it does suggest that their effects on the temperature structure are small. In our model equally good fits can be obtained whether or not a methane condensation cloud is included. Our results are in agreement with those of Toon *et al.* (1988) in that the presence of a condensation cloud does result in a slightly better fit to the IRIS data. The thermal structure of the atmosphere is also largely independent of the relative humidity of the surface. This is due to the fact that the methane concentration is set by its saturation vapor pressure in all but the lower few kilometers of the atmosphere. Thus our results are insensitive to the presence or composition of an ethane rich surface ocean. The greenhouse effect observed on Titan can be accounted for by absorption at the ground of about 10% of the solar energy incident on Titan. The high stratospheric temperatures are due to absorption of short wavelength solar energy by the haze particles. The surface is warmed in approximately equal amounts by solar radiation of wavelengths less than 0.7 and greater than 1  $\mu\text{m}$ .

The stratospheric haze on Titan dominates the transfer of solar radiation in the atmosphere. We have found that the tholin particles produced in the laboratory (Khare *et al.* 1984) are good optical analogs to the Titan haze particles. In addition we have found that the haze production rate,  $1.2 \times 10^{-14} \text{ g cm}^{-2} \text{ sec}^{-1}$ , is less than previous models would suggest.

An important, if not primary, key to understanding the thermal structure of Titan's atmosphere is the thermal infrared optical properties. The presence of a "window" at 400–600  $\text{cm}^{-1}$  in the thermal infrared has a major influence on the temperature structure of Titan's atmosphere. Our results indicate that the baseline estimates derived from the work of Courtin (1988) for the total opacity in this spectral region, less than unity and as low as 0.3—in the absence of a

condensation cloud—are probably too low, perhaps by a factor of 2. We found improved agreement with the observations if we increased these results by 75% for infrared wavenumbers larger than 300  $\text{cm}^{-1}$ . The presence of a cloud alone is not sufficient to close the infrared window since for cloud particles sizes consistent with solar energy deposition, and optical thicknesses consistent with the IRIS spectra, the cloud mostly scatters thermal infrared radiation and has only a small net effect.

The window region, along with the strong gas opacity at wavenumbers near 100–200  $\text{cm}^{-1}$ , acts to stabilize Titan's surface temperature. If the temperature were to decrease, the thermal infrared emission peak would move into a wavelength region of greater opacity, thereby limiting the decrease in temperature. Conversely if the temperature were to increase, the thermal infrared emission peak would move into a region of lesser opacity, thereby cooling the surface.

#### APPENDIX: MODEL DESCRIPTION

We have developed a radiative–convective model of the thermal structure of Titan's atmosphere by dividing the atmosphere into a series of plane parallel homogeneous layers. There are 30 layers spaced in altitude such that the size of each layer increases linearly with altitude. The thickness of the bottom layer is  $\sim 1 \text{ km}$  and the uppermost layers are 15 times as thick. To compute the radiative fluxes the model considers 24 spectral intervals in the visible from 0.3 to 2.3  $\mu\text{m}$  and 46 spectral intervals in the thermal infrared from 11 to 940  $\text{cm}^{-1}$  ( $\lambda \approx 10\text{--}900 \mu\text{m}$ ). The model begins with the Voyager Titan atmosphere as the initial atmospheric profile and computes the net radiative flux at the boundary between adjacent layers. This is used to diagnose the sources and sinks of energy in the present Titan atmosphere. The model is then allowed to relax to a temperature profile that results in a zero net flux across each level subject to the condition of convective ad-

TABLE IV  
MOLECULAR REFRACTIVITIES OF GASES IN TITAN'S ATMOSPHERE

Gas	Refractivity [ $(n - 1) \times 10^6$ ]	Wavelength <sup>a</sup>	Reference
N <sub>2</sub>	294.1 ± 0.1	3.3 cm	Essen (1953)
CH <sub>4</sub>	410 ± 17	337 μm	Kutovoi <i>et al.</i> (1975)
H <sub>2</sub>	136.0 ± 0.2	3.3 cm	Essen (1953)
Ar	277.8 ± 0.2	1.3 cm	Essen and Froome (1951)

<sup>a</sup> The radio occultation measurements were made at 3.6 and 13 cm.

justment if the lapse rate exceeds the dry N<sub>2</sub> lapse rate. The distribution of condensable gases and the implied optical properties are updated as the temperature changes.

**Voyager results.** The Voyager Titan atmospheric temperature profile is determined from the egress data of Lindal *et al.* (1983) corrected for the presence of gases other than nitrogen in an iterative procedure, as follows. First the egress temperature profile is used to compute a methane mixing ratio. Together with a specified distribution of argon (usually zero) and hydrogen (usually 0.3%) this determines the mean molecular weight profile. Using the refractivities listed in Table IV, the egress density profile of Lindal *et al.* (1983) is recomputed to correct for the presence of nonnitrogen gases. The new density profile and the new mean molecular weights are then used to compute new values of pressure and temperature based on the hydrostatic law and the nonideal Benedict-Webb-Rubin equation of state for methane and nitrogen (Ellington *et al.* 1959, Reid *et al.* 1977). Argon and hydrogen were treated using the coefficients for nitrogen in the equation of state.

**Gases.** The methane distribution is determined by the temperature profile and by the relative humidity at the surface. Above the surface, the methane mixing ratio is held constant until the local partial pressure exceeds the methane vapor pressure. The

methane mixing ratio then remains saturated until the minimum mixing ratio is reached (~1.7% at 30 km). This minimum mixing ratio is continued through the stratosphere. Hydrogen is assumed to have a constant mixing ratio throughout the atmosphere. The surface relative humidity of methane and the hydrogen mixing ratio were determined by fitting the thermal emission in the 200–600 cm<sup>-1</sup> region with the Voyager IRIS results as described below and considered in more in detail by Toon *et al.* (1988). Following Toon *et al.* (1988) we do not include argon in the Titanian atmosphere.

The radiatively active trace gases in the model are assumed to have constant mixing ratios in the stratosphere (C<sub>2</sub>H<sub>2</sub>:  $1.8 \times 10^{-6}$  and C<sub>2</sub>H<sub>6</sub>:  $1.2 \times 10^{-5}$ ) set by Voyager observations (Kunde *et al.* 1981, Coustenis *et al.* 1989). HCN is not included since it overlaps with but is weaker than C<sub>2</sub>H<sub>2</sub> and C<sub>2</sub>H<sub>6</sub> in the spectral intervals we have used. The CH<sub>4</sub> features at 1300 cm<sup>-1</sup> are not included since it contributes only a small amount to the total emission (see, e.g., Fig. 2 of Kunde *et al.* 1981). Near the cold trap the mixing ratios of these gases are set by saturation and in the troposphere the minimum value of the mixing ratio is extended to the ground; i.e., the mixing ratio is constrained not to increase with decreasing altitude. This profile is consistent with a stratospheric source. The vapor pressure curves for C<sub>2</sub>H<sub>2</sub> and C<sub>2</sub>H<sub>6</sub>, for temperatures below

200°K, are adapted from the formulas and tables in Ziegler (1959). They are expressed in the form  $P = ae^{b/r}$ , where  $a$  and  $b$  are, for ethane,  $5.02 \times 10^8$  mb and  $-2222.9^\circ\text{K}$ , respectively, and for acetylene;  $3.46 \times 10^9$  mb and  $-2814.0^\circ\text{K}$ , respectively. Methane vapor pressure was determined by a fit to data over the range  $74\text{--}98^\circ\text{K}$  (Matheson 1974) yielding  $a = 3.45 \times 10^7$  mb and  $b = -1145.7^\circ\text{K}$ .

**Haze.** We have used a simple haze model to determine the aerosol size and optical depth given the particle charging and production rate as a function of altitude. Our steady-state model is based on assuming that (1) all the particles at a given altitude have the same radius, and (2) only coagulation and sedimentation are considered within homogeneous layers.

The basic equations that determine the haze properties are conservation of mass and number. The conservation of mass equation, exact if  $r$  is the volume mean radius, is given by

$$-nvr^3 \frac{4}{3} \pi \rho = \int_z^\infty q(z) dz = C(z), \quad (1)$$

where  $v$  is the settling velocity,  $n$  is the particle number density,  $\rho$  is the bulk density of the particle material,  $q$  is the production rate, and  $C(z)$  is the column production rate above the altitude,  $z$ . Since we have assumed that only coagulation affects the number of particles we can write an equation for the flux of particles, based on Eq. (1) of Toon *et al.* (1980), with the divergence of the sedimentation number flux set equal to the coagulation term. We obtain

$$\frac{d(nv)}{dz} = -Kn^2, \quad (2)$$

where  $K$  is the coagulation coefficient.

We now solve these equations by making use of the following expressions (Toon *et al.* 1980), valid for the case in which the mean free gas path is much larger than the particle size:

$$v = -br \quad (3)$$

$$K = a\sqrt{r}, \quad (4)$$

where

$$b = \frac{\rho g}{2n_a} \left( \frac{\pi}{2m_a kT} \right)^{1/2}$$

and

$$a = 4 \left[ \frac{3kT}{\rho} \right]^{1/2},$$

both assumed constant within an individual layer, and where  $g$  is the gravitational acceleration,  $n_a$  and  $m_a$  are the atmospheric number density and mean molecular weight, respectively,  $k$  is Boltzmann's constant, and  $T$  is the temperature.

Solving the above set of equations gives

$$\frac{dr^{9/2}}{dz} = \frac{-9}{8\pi\rho b} \left[ \frac{aC(z)}{b} + \frac{q(z)\sqrt{r}}{n} \right]. \quad (5)$$

For most of the atmosphere  $q(z) = 0$  and  $C(z) = C_0$ , where  $C_0$  is the total column production. Equation (5) then becomes

$$\frac{dr^{9/2}}{dz} = \frac{-9aC_0}{8\pi\rho b^2}. \quad (6)$$

Given this equation for  $dr/dz$  and an initial value for  $r$  at the top of the atmosphere, we can solve stepwise for  $r$  at all the levels in the model. The results are not sensitive to the choice of the radius at the top of the model if it is a small value and if the upper boundary is above the haze production region. The density,  $n$ , is obtained from Eq. (1).

Low in the atmosphere the assumption of large mean free path breaks down and it would be more appropriate to use the equations for sedimentation and coagulation valid for the Stokes regime (see, e.g., Borucki *et al.* 1984). These approximations are incorporated into the algorithm by allowing the values  $b$  in Eq. (3) and  $a$  in Eq. (4) to vary smoothly toward their Stokes regime values as the ratio of the mean free path to particle size decreases ( $b = 2\rho gr/9\eta$ ,  $a = (4kT/3\eta\sqrt{r})$ , where  $\eta$  is the viscosity).

Following Toon *et al.* (1980) we represent the production term  $q$  as

$$q = q_0 \exp \left\{ -\frac{1}{2} \left[ \frac{(P - P_0)}{P_y} \right]^2 \right\}, \quad (7)$$

where  $P_0$  is the pressure of maximum haze production and  $P_y$  is the pressure range over which haze production occurs. Using the values listed in Table I of Toon *et al.* (1980) this simple model can duplicate with good agreement the "base case" from that paper.

To account for the effect of electrostatic forces between particles we assume that the particles have constant charge per unit radius (Borucki *et al.* 1987) and utilize the formalization of Turco *et al.* (1982) to derive a reduction factor for the coagulation coefficient. This is incorporated into the results by replacing  $a$  with  $ae^{-r/r_c}$  in the above equations, where  $r_c$  is the radius (constant) at which the reduction is a factor of  $e$ .

The advantages of this simple model over merely specifying particle size and density profiles is that the adjustable parameters in the model can be related to physically meaningful quantities such as haze production magnitude and distribution and the number of free parameters is greatly reduced. To accurately model the haze the preceding equations are solved on a pressure-temperature grid that differs from the grid used in the radiative-convective calculations in two ways. First, since all the haze production occurs above the top of the radiative-convective grid the haze grid extends to almost 700 km, well above the maximum height of peak haze production ( $\sim 550$  km,  $P \approx 10^{-4}$  mb). Secondly, the haze grid has a larger number of layers uniformly spaced, resulting in relatively more grid points at the upper reaches of the model where the haze is produced. The haze density and particle size are then interpolated onto the background grid. Below the uppermost level of methane condensation ( $\sim 30$  km) the haze is assumed to be swept clear.

*Radiative transfer methods.* The radiative transfer equation for both the solar and thermal infrared is solved by different variants of the two stream approximation. The solar spectrum is divided into 24 spectral intervals; the only gaseous absorber considered is methane. The methane absorption within each spectral interval has a complex band structure, especially at the longer wavelengths, that cannot be treated simply by the use of monochromatic absorption coefficients. Band models can be used to express the gaseous absorption but they do not allow for solution of the radiative transfer equation with scattering (see, e.g., Ackerman *et al.* 1976, Pollack and McKay 1985). A similar problem occurs for terrestrial absorbers and our approach follows that of Pollack and McKay (1985) in that the methane absorption is expressed within each spectral interval by a weighted sum of exponentials.

The transmission,  $T$ , as a function of absorber column mass,  $u$ , within a layer for a given spectral interval is expressed as

$$T(u) = \sum_i w_i e^{-k_i u}, \quad (8)$$

where the  $w_i$  are weights and the  $k_i$  are equivalent monochromatic absorption coefficients. The absorption coefficients are scaled by the factor  $P^n$  where  $P$  is the pressure in atmospheres and  $n$  is a constant, different for each spectral interval. Table V lists the midpoint wavelengths of the spectral intervals used in the model and the corresponding values of  $w_i$ ,  $k_i$ , and  $n$ . The values of  $w_i$ ,  $k_i$ , and  $n$  were obtained by K. A. Rages by fitting the average transmission over each wavelength interval at a number of different column abundances and pressures. The average transmissions for each wavelength interval were calculated as the trapezoidal sums of transmissions over  $\sim 2$  nm intervals. For wavelengths less than  $1.08 \mu\text{m}$  the transmissions were calculated using the absorption coefficients of Giver (1978). Longward of  $0.853 \mu\text{m}$  these absorption coefficients were combined with



TABLE V  
SPECTRAL INTERVALS IN VISIBLE AND METHANE EXPONENTIAL-SUM ABSORPTION COEFFICIENTS

$\lambda$ ( $\mu\text{m}$ )	Solar flux ( $\text{erg cm}^{-2} \text{sec}^{-1}$ )	Pressure exponent	Weights	Monochromatic absorption coefficients ( $\text{g}^{-1} \text{cm}^2$ )				
0.325	525.43	0	1.000	0	0	1.096E - 5	3.249E - 5	7.717E - 5
0.375	680.44	0	1.000	0	0	1.321E - 5	6.405E - 5	5.977E - 4
0.425	1051.90	0	0.700	0.191	0	3.548E - 5	2.103E - 4	1.254E - 3
0.475	1173.30	0	0.300	0.135	0	2.730E - 6	2.159E - 4	4.466E - 4
0.525	1082.00	0	0.164	0.375	0.165	3.560E - 5	3.641E - 4	1.360E - 3
0.575	1056.50	0	0.445	0.356	0.199	1.004E - 4	2.625E - 3	1.106E - 2
0.640	1495.10	0	0.198	0.332	0.134	6.237E - 4	2.722E - 3	1.115E - 2
0.715	1123.10	0	0.327	0.336	0.147	7.969E - 4	6.944E - 3	3.216E - 2
0.789	1053.20	0	0.277	0.333	0.390	4.367E - 4	1.995E - 1	1.970
0.850	541.82	0.149	0.127	0.416	0.365	1.784E - 2	8.659E - 3	9.687E - 2
0.891	397.63	0.156	0.286	0.492	0.221	1.318E - 3	1.758E - 1	2.062
0.935	484.21	0.186	0.445	0.454	0.101	2.617E - 2	1.314E - 2	5.890E - 2
0.998	624.54	0.302	0.351	0.372	0.277	1.904E - 3	1.851E - 2	3.179E - 1
1.073	528.39	0.097	0.434	0.477	0.078	8.582E - 4	8.488E - 3	5.583E - 1
1.144	383.25	1.150	0.292	0.374	0.242	0	8.519E - 3	6.320E - 1
1.213	372.26	1.040	0.502	0.386	0.113	0	2.719E - 2	4.479E - 1
1.292	360.09	1.030	0.597	0.308	0.095	3.807E - 3	8.182E - 3	7.091E - 1
1.381	339.23	1.040	0.117	0.447	0.338	0	1.097E - 2	4.988E - 1
1.484	315.60	1.080	0.541	0.368	0.091	8.809E - 5	4.319E - 1	6.510
1.603	292.58	1.070	0.468	0.213	0.106	2.475E - 2	9.376E - 3	6.444E - 1
1.742	267.60	1.090	0.245	0.417	0.243	0	1.028E - 2	5.555E - 1
1.909	239.70	1.050	0.330	0.504	0.166	0	5.285	7.158E + 1
2.111	208.04	1.050	0.308	0.361	0.232	0	1.343E - 1	4.469E + 1
2.361	180.55	0.959	0.116	0.353	0.413	0.118	5.285	3.912E + 3

the pressure coefficients of Fink *et al.* (1977) in a Goody random band model with Voigt line profiles and an exponential distribution of line intensities [Eq. (9) of Podolak and Giver (1979)]. For the spectral region 4000–9000  $\text{cm}^{-1}$  the absorption coefficients and pressure coefficients found by Benner and Fink (1980) were used in the same type of band model. To bridge the small gap between these two data sets a line-by-line calculation of the R-branch of the  $3\nu_3$  band was carried out, including line positions and strengths calculated by L. Giver for the weaker lines, as well as the major components.

Within each spectral interval the equation of transfer was solved up to four times as a monochromatic equation of transfer, once for each term in the expansion in Eq. (8), with the particle and Rayleigh optical properties identical for each of the four computations. The four fluxes thus obtained were then summed with the terms scaled by the values of  $w_i$  to give the total flux in the spectral interval. The solar flux values listed in Table V were divided by 4 to represent globally averaged conditions. Rayleigh scattering is important at the shorter wavelengths considered and is expressed following the formula of Hansen and Travis (1974).

Particles and clouds were treated as spherical Mie scatters both in the visible and in the thermal infrared. The only laboratory data available on the optical constants of haze-like particles is that of Khare *et al.* (1984). Their values for the real part of the index of refraction are used both in the solar and in the thermal infrared. The imaginary part of the index of refraction of the haze was determined by fitting a scale factor (§) to the results of Khare *et al.* (1984) as described below. The real index of refraction of methane clouds was assumed to be 1.27 both at solar and thermal infrared wavelengths. Absorption by methane clouds was neglected in the visible (the imaginary part of the index of refraction

was set to  $10^{-7}$ ). In the thermal infrared, the imaginary part of the index of refraction of methane cloud particles was the same as that adopted by Toon *et al.* (1988).

Gaseous absorption in the thermal infrared is dominated by pressure-induced absorption (see, e.g., Courtin 1982, 1988, Thompson and Sagan 1984). Due to the absence of laboratory data there was considerable uncertainty in the semi-empirical methods previously used to compute the pressure induced absorption coefficients. Recently, Courtin (1988) has reviewed new laboratory data and suggested improved parameters for the coefficients, most noticeably for the  $\text{N}_2\text{--H}_2$  term. Among other things, these changes significantly effect the strength of the  $\text{H}_2$  spectral feature near 600  $\text{cm}^{-1}$ . For computational speed the values of the pressure-induced absorption coefficients are interpolated from precomputed values spaced in 10°K intervals from 60 to 190°K for the center wavenumber of each spectral interval in the thermal infrared. Although argon is not included in the atmosphere, it would not significantly alter the pressure-induced gas opacity since  $\text{N}_2\text{--Ar}$  interactions result in values very similar to those of  $\text{N}_2\text{--N}_2$ , already in the model (Courtin 1988). The pressure-induced opacity within each homogeneous atmospheric layer represents true continuum absorption and within each spectral interval can be characterized by a single monochromatic absorption coefficient following Beer's law.

The IRIS spectra of Titan (Hanel *et al.* 1981) show that stratospheric gases contribute a non-negligible fraction of the energy emitted to space and hence must play a role in the stratospheric heat budget. Stratospheric gases of interest include HCN (645–740  $\text{cm}^{-1}$ ),  $\text{C}_2\text{H}_2$  (645–815  $\text{cm}^{-1}$ ),  $\text{C}_2\text{H}_6$  (740–940  $\text{cm}^{-1}$ ), and  $\text{CH}_4$  (1100–1750  $\text{cm}^{-1}$ ). We have developed multi-term exponential-sum band models for these gases in which the monochromatic absorption coefficient ( $k_i$ ) as defined in Eq. (8) is expressed as

$$\ln(k_i) = a_1 + a_2 \ln(T) + a_3 \ln(T)^2 \\ + [b_1 + b_2 \ln(T) + b_3 \ln(T)^2] \ln\left(\frac{P}{P_0}\right) \\ + [c_1 + c_2 \ln(T) + c_3 \ln(T)^2] \ln\left(\frac{P}{P_0}\right)^2, \quad (9)$$

where  $P_0 = 100$  mb is a reference pressure and the  $a$ ,  $b$ , and  $c$  terms are constants determined by a fit to "line by line" computations based on line strengths and positions given on the Air Force Cambridge Laboratory tapes. These line by line calculations were done for grids of temperature, pressure, and gas amount that encompassed ranges of interest for modeling Titan. For the temperature and column mass paths of gases determined by IRIS in the stratosphere,  $C_2H_2$  and  $C_2H_6$  are the dominant absorbers in the wavenumber intervals from 645 to 740  $cm^{-1}$  and 740 to 940  $cm^{-1}$ , respectively (HCN is omitted). The  $C_2H_2$ ,  $C_2H_6$  coefficients for the exponential terms that were used are listed in Table VI for each wavelength interval. The weights are based on a 10-point Gaussian fit to the cumulative  $k$  probability distribution and are equivalent to the fraction of the flux in the

spectral interval that corresponds to the given absorption coefficient (see Table VI). An accuracy of better than 1% was achieved in these bands with the first few terms in a 10 exponential sum and combining the additional terms into a single term corresponding to a zero absorption coefficient. The opacity of the  $C_2H_2$  or  $C_2H_6$  gas band is added to the pressure-induced gaseous opacity.

The various sources of extinction and scattering for each layer are then summed, weighted by the opacity, into layer averages. The scattering and absorption coefficients of the cloud particles and the haze were computed with Mie theory (e.g., Liou 1980).

The procedure outlined above results in the layer extinction,  $\tau$ , the layer single scattering albedo,  $\bar{\omega}$ , and the layer asymmetry factor,  $\langle\theta\rangle$ , for both the solar and thermal infrared spectral intervals. These values are then used to compute the fluxes at each layer. In the solar spectrum the delta-discrete ordinates method was used (e.g., Liou 1980, Meador and Weaver 1980, Toon *et al.* 1989). In the thermal infrared the hemispheric constant method for treating scattering developed by Pollack and

TABLE VI

SPECTRAL INTERVALS AND EXPONENTIAL-SUM ABSORPTION COEFFICIENTS FOR STRATOSPHERIC GASES

Interval ( $cm^{-1}$ )	Gas	Weight	$a_1$	$a_2$	$a_3$	$b_1$	$b_2$	$b_3$	$c_1$	$c_2$	$c_3$
645-685	$C_2H_2$	0.03334	-58.078	31.248	-6.158	5.278	-4.004	0.820	-8.997	8.439	-1.991
		0.07473	-73.670	45.093	-9.478	2.667	-1.494	0.323	6.517	-6.630	1.644
		0.03334	-22.004	3.537	-0.726	1.317	-0.801	0.162	-0.549	0.487	-0.132
685-720	$C_2H_2$	0.07473	-26.612	7.342	-1.738	-5.053	5.866	-1.423	-4.805	4.439	-1.027
		0.10954	-27.040	7.098	-1.658	1.880	-0.960	0.260	2.830	-3.215	0.808
		0.13463	-25.840	5.353	-1.238	4.493	-3.388	0.874	-2.120	1.926	-0.500
		0.03334	-18.703	1.585	-0.337	-0.947	1.248	-0.316	-1.532	1.339	-0.306
720-740	$C_2H_2$	0.07473	-16.084	-2.630	0.843	2.775	-1.759	0.369	-13.483	12.548	-2.918
		0.10954	-23.033	2.881	-0.442	15.806	-13.075	2.867	-18.913	17.742	-4.145
		0.13463	-31.183	11.386	-2.791	33.831	-29.975	6.837	-16.896	14.035	-2.915
		0.03334	-19.965	0.335	0.003	-2.295	2.674	-0.757	-1.024	0.846	-0.181
		0.07473	-24.375	3.361	-0.602	2.908	-1.738	0.242	0.257	-0.303	0.070
740-815	$C_2H_6$	0.10954	-17.944	-3.943	1.278	0.773	0.879	-0.461	-6.276	5.989	-1.435
		0.03334	-17.463	-1.570	0.377	-0.955	1.356	-0.427	-0.567	0.409	-0.076
		0.07473	-20.938	0.288	0.088	3.305	-2.090	0.329	0.147	-0.174	0.037
		0.10954	-10.744	-10.550	2.777	0.439	1.404	-0.614	-8.537	8.137	-1.938

TABLE VII  
WAVELENGTHS AND MONOCHROMATIC ABSORPTION  
COEFFICIENTS USED TO COMPUTE  
GEOMETRIC ALBEDO

Wavelength ( $\mu\text{m}$ )	Absorption coefficient at 95°K, $k$ ( $\text{km-amagats}$ ) <sup>-1</sup>	Note
0.200	0 <sup>a</sup>	
0.250	0 <sup>a</sup>	
0.300	0 <sup>a</sup>	
0.350	0 <sup>b</sup>	
0.450	0.0008 <sup>a</sup>	
0.550	0.003 <sup>b</sup>	
0.580	0.0191 <sup>a</sup>	
0.620	0.53 <sup>b</sup>	
0.636	0.0051 <sup>a</sup>	
0.728	3.95 <sup>b</sup>	
0.750	0.0015 <sup>b</sup>	0.02 <sup>c</sup>
0.799	1.23 <sup>b</sup>	
0.827	0.011 <sup>b</sup>	0.04 <sup>c</sup>
0.841	0.918 <sup>a</sup>	
0.862	5.28 <sup>a</sup>	
0.888	34.0 <sup>b</sup>	
0.935	0.077 <sup>a</sup>	

<sup>a</sup> K. Rages, personal communication.

<sup>b</sup> Pollack *et al.* (1986).

<sup>c</sup> Room temperature value used in determining  $k$  at 95°K.

McKay (1985) is used. As discussed by Toon *et al.* (1989) this method is optimal for the thermal infrared because of the isotropic nature of the Planck function. In this approach the Planck function term in the source function is approximated as  $B(\tau) = B_0 + B_1\tau$  where  $B_0$  and  $B_1$  are constants within each layer and  $\tau$  is the optical depth in that layer for the spectral interval under consideration. The individual solutions for the many layers in the atmosphere together form a coupled set of algebraic equations. Together with the appropriate boundary conditions these equations form a matrix equation that can be solved for the coefficients of the two-stream solution within each layer. We use the computationally efficient algorithm developed by Toon *et al.* (1989) to solve the resulting matrix equation.

The two-stream method is well suited to rapid computation of fluxes and heating rates. In addition, the errors introduced by the two-stream approximation (typically less than 10%; see, e.g., Toon *et al.* 1989) are small compared to the uncertainties in the physical properties of Titan's atmosphere. However, one of the key data sets that will help us constrain the free parameters in the model is the spectrally resolved geometric albedo. The geometric albedo cannot be computed with a two-stream method. To compute the geometric albedo we use the Eddington source function method as described by Toon *et al.* (1989), with 10 Gauss point integration over angle (see also Appendix A of Toon *et al.* 1977 for a similar method). In this method the source function from the Eddington two-stream is used in an exact integral of the radiative transfer equation in order to compute emergent intensities. Toon *et al.* (1989) present a detailed discussion of the errors associated with the radiative transfer methods used in this paper.

**Matrix solution method.** The model is divided into a series of "layers" with "levels" as the interfaces between the layers. The temperature is specified at each level. The fluxes within each layer are solved to give an analytic expression as a function of optical depth within the layer. Thus the program can compute fluxes at the levels and at the midpoints of each layer. We use the midpoint fluxes as matched variables with the level temperatures. This staggering of temperature and flux calculation points appears to be a requirement for a well-behaved solution in radiative-convective models.

Physically the model has two regions: a troposphere and a stratosphere. The troposphere is the lower portion of the model and is in convective equilibrium while the stratosphere is the upper portion and is in radiative equilibrium. The level at which the split occurs is defined to be  $N_0$ . Hence all layers above  $N_0$  are in radiative equilibrium and all layers below  $N_0$  are in convec-

tive equilibrium. The objective of the radiative-convective model is to determine the correct level for  $N_0$  and to calculate the resulting temperature profile. This is achieved by satisfying the following two criteria: (1) All layers above the level  $N_0$  have stable lapse rates and zero net radiative fluxes across their midpoints. There is zero net flux at the top of the atmosphere. All layers below level  $N_0$  have a lapse rate defined by convective equilibrium. (2) The level of  $N_0$  is the lowest altitude that is consistent with constraint 1.

The fluxes at each midpoint depend, in principal, on the temperatures in the entire atmosphere since there is radiative exchange between nonadjacent layers. The problem is equivalent to a set of equations for the fluxes as function of the temperatures. So,

$$F_i = F_i(T_1, T_2, T_3, \dots, T_{N_0}), \quad (10)$$

where  $F_i$  is the flux at the midpoint of layer  $i$ , and  $T_i$  is the temperature at the level  $i$ , which is also the top of layer  $i$ . The fluxes in the stratosphere are clearly influenced by the temperature profile in the troposphere but since the troposphere temperature profile is uniquely determined by  $T_{N_0}$  only this term appears as an independent variable. Apparently the problem is much better conditioned if the fluxes are determined on a grid staggered with respect to the temperature grid. For this reason the fluxes are calculated at the midpoints of the layers (recall that the temperatures are specified at the levels, which are the edges of each layer). However, this does pose a slight problem in that there are  $N_0$  levels in the stratosphere but only  $N_0 - 1$  layer midpoints. To have a match between the number of dependent and independent variables we need to include either the net flux at the top of the stratosphere or at the bottom. We use the top. Thus our variables form two vectors of length  $N_0$ . They are, in order,

$$T: T_1, T_2, T_3, \dots, T_{N_0} \quad (11)$$

and

$$F: F_{\text{top}}, F_1, F_2, \dots, F_{N_0-1}. \quad (12)$$

The radiative equilibrium profile for the stratosphere is determined by the  $T_i$ 's that will make all the  $F_i$ 's zero. This is done by iteration in the following manner: (1) An initial guess for the temperature profile is entered. (2) The fluxes are calculated and the net flux at the top of the atmosphere and at each midpoint in the stratosphere is determined. In general these will not be zero. These residual fluxes are labeled  $R_i$ . (3) We add small changes  $\delta T_i$  to each temperature variable  $T_i$  chosen such that the resulting change in each  $F_i$  is the negative of  $R_i$ .

We determine the  $\delta T_i$  for step (3) in the following approximate manner. Consider the dependent variables

$$F_i = F_i(T_1, T_2, T_3, \dots, T_{N_0}) \quad (13)$$

and their differentials with respect to temperature:

$$dF_i = \frac{\partial F_i}{\partial T_1} \delta T_1 + \frac{\partial F_i}{\partial T_2} \delta T_2 + \frac{\partial F_i}{\partial T_3} \delta T_3 + \dots \quad (14)$$

If we consider all  $F_i$ , clearly we can write this set of equations as a matrix equation as so:

$$dF = A \times \delta T, \quad (15)$$

where  $dF$  and  $\delta T$  are vectors of length  $N_0$  and  $A$  is a square matrix of order  $N_0$ . Clearly  $A$  is the Jacobian matrix defined by

$$A_{ij} = \frac{\partial F_i}{\partial T_j}. \quad (16)$$

Our objective here is to pick the  $\delta T$  vector such that  $dF_i = -R_i$ . Then when we increment the temperature profile by  $T_i = T_i + \delta T_i$  the new fluxes should be zero, or close to zero in the sense that the procedure above is approximate. We then solve the matrix equation,

$$-R = A \times \delta T, \quad (17)$$

for  $\delta T$ .

In order to calculate the Jacobian matrix  $A$  we use a numerical approach. We incre-

ment (by  $\Delta T \sim 1^\circ\text{K}$ ) one and only one temperature point, say  $T_j$  (if this temperature is the temperature at level  $N_0$  then all the troposphere temperatures change also), and then we recalculate all the fluxes based on this new perturbed temperature profile ( $F^p$ ). We then calculate the matrix terms as follows:

$$A_{ij} = \frac{F_i^p - F_i}{\Delta T}, \quad (18)$$

where the  $j$  value is determined by which temperature point was perturbed, and the term  $F_i$  is the flux determined from the unperturbed temperature profile. The perturbation is removed, a new temperature point is perturbed and the procedure is repeated for each temperature point. Note that in addition to the initial unperturbed flux calculation the fluxes must be recalculated  $N_0$  times, once for each temperature point.

The numerical procedure is approximate and depending on the matrix solver used several iterations may be required to achieve a good solution in which the net fluxes are very small. We have used the matrix solver LEQ2TF from the IMSL library to achieve flux convergences of  $\sim 0.1\%$  or better with about five iterations on the final value of  $N_0$ .

#### ACKNOWLEDGMENTS

We thank Brian Toon for numerous useful discussions and suggestions regarding our results and for access to unpublished results critical to the model development and validation. We thank Kathy Rages for providing the methane exponential-sum parameters and Kathy Poliakoff for allowing us to use her exponential fits for the stratospheric gases. We thank John Caldwell for a thorough and helpful review of the manuscript.

#### REFERENCES

- ACKERMAN, T. P., K. N. LIOU, AND C. B. LEOVY 1976. Infrared radiative transfer in polluted atmospheres. *J. Appl. Meteorol.* **15**, 28–35.
- BENNER, D. C., AND U. FINK 1980. Analysis of infrared laboratory  $\text{CH}_4$  spectra. *BAAS* **12**, 697.
- BORUCKI, W. J., C. P. MCKAY, AND R. C. WHITTEN 1984. Possible production by lightning of aerosols and trace gases in Titan's atmosphere. *Icarus* **60**, 260–273.
- BORUCKI, W. J., Z. LEVIN, R. C. WHITTEN, R. G. KEESEE, L. A. CAPONE, A. L. SUMMERS, O. B. TOON, AND J. DUBACH 1987. Predictions of the electrical conductivity and charging of the aerosols in Titan's atmosphere. *Icarus* **72**, 604–622.
- CHANG, S., T. SCATTERGOOD, A. ARONOWITZ, AND J. FLORES 1979. Organic chemistry on Titan. *Rev. Geophys. Space Phys.* **17**, 1923–1933.
- COURTIN, R. 1982. The spectrum of Titan in the far-infrared and microwave regions. *Icarus* **51**, 466–475.
- COURTIN, R. 1988. Pressure induced absorption coefficients for radiative transfer in Titan's atmosphere. *Icarus* **75**, 245–254.
- COUSTENIS, A., B. BÉZARD, AND D. GAUTIER, 1989. Titan's atmosphere from Voyager infrared observations. *Icarus*, in press.
- DANIELSON, R. E., J. J. CALDWELL, AND D. R. LARACH 1973. An inversion in the atmosphere of Titan. *Icarus* **20**, 437–443.
- ELLINGTON, R. T., O. T. BLOOMER, B. E. EAKIN, AND D. C. GAMI 1959. Thermodynamic properties of methane–nitrogen mixtures. In *Thermodynamic and Transport Properties of Gases, Liquids and Solids* (Y. S. Touloukian, Ed.), pp. 102–109. McGraw-Hill, New York.
- ESHLEMAN, V. R., G. F. LINDAL, AND G. L. TYLER 1983. Is Titan wet or dry? *Science* **221**, 53–55.
- ESSEN, L. 1953. The refractive indices of water vapor, air, oxygen, nitrogen, hydrogen, deuterium and helium. *Proc. Phys. Soc.* **66**(B), 189–193.
- ESSEN, L., AND K. D. FROOME 1951. The indices and dielectric constants of air and its principle constituents at 24,000 Mc/s. *Proc. Phys. Soc.* **64**(B), 862–875.
- FINK, U., D. C. BENNER, AND K. A. DICK 1977. Band model analysis of laboratory methane absorption spectra from 4500 to 10,500 Å. *J. Quant. Spectrosc. Radiat. Transfer* **18**, 447–457.
- FINK, U., AND H. P. LARSON 1979. The infrared spectra of Uranus, Neptune, and Titan from 0.8 to 2.5 microns. *Astrophys. J.* **233**, 1021–1040.
- FLASAR, F. M. 1983. Oceans on Titan? *Science* **221**, 55–57.
- GIVER, L. P. 1978. Intensity measurements of the  $\text{CH}_4$  bands in the region 4350 to 10,600 Å. *J. Quant. Spectrosc. Radiat. Transfer* **19**, 311–322.
- HANEL, R., B. CONRATH, F. M. FLASAR, V. KUNDE, W. MAGUIRE, J. PEARL, J. PIRRAGLIA, R. SAMUELSON, L. HERATH, M. ALLISON, D. CRUIKSHANK, D. GAUTIER, P. GIERASCH, L. HORN, R. KOPPANY, AND C. PONNAMPERUMA 1981. Infrared observations of the Saturnian system from Voyager 1. *Science* **212**, 192–200.
- HANSEN, J. E., AND L. D. TRAVIS 1974. Light scattering in planetary atmospheres. *Space Sci. Rev.* **16**, 527–610.
- KHARE, B. N., C. SAGAN, E. T. ARAKAWA, F. SUITS, T. A. CALLCOTT, AND M. W. WILLIAMS 1984. Optical constants of organic tholins produced in a simu-

- lated Titanian atmosphere: From soft X-ray to microwave frequencies. *Icarus* **60**, 127–137.
- KUNDE, V. G., A. C. AIKIN, R. A. HANEL, D. E. JENNINGS, W. C. MAGUIRE, AND R. E. SAMUELSON 1981.  $C_4H_2$ ,  $HC_3N$ , and  $C_2N_2$  in Titan's atmosphere. *Nature* **292**, 686–688.
- KUTOVOI, V. D., G. D. PETROV, P. A. SAMARSKII, AND S. I. TREGUBOV 1975. Submillimeter plasma interferometry at two wavelengths. *Sov. J. Plasma Phys.* **1**, 470–472.
- LINDAL, G. F., G. E. WOOD, H. B. HOTZ, D. N. SWEETNAM, V. R. ESHLEMAN, AND G. L. TYLER 1983. The atmosphere of Titan: An analysis of the Voyager 1 radio occultation measurements. *Icarus* **53**, 348–363.
- LIU, K. 1980. *An Introduction to Atmospheric Radiation*. Academic Press, New York.
- LUNINE, J. I., D. J. STEVENSON, AND Y. YUNG 1983. Ethane oceans on Titan. *Science* **222**, 1229–1230.
- Matheson Gas Co. 1974. *The Matheson Unabridged Gas Data Book*. Matheson Gas Products.
- MEADOR, W. E., AND W. R. WEAVER 1980. Two-stream approximations to radiative transfer in planetary atmospheres: A unified description of existing methods and a new improvement. *J. Atm. Sci.* **37**, 630–643.
- McKAY, C. P., AND J. B. POLLACK 1984. The role of scattering in the infra-red on the heat budget of Titan's lower atmosphere. *BAAAS* **16**, 665.
- NEFF, J. S., T. A. ELLIS, J. APT, AND J. T. BERGSTRALH 1985. Bolometric albedos of Titan, Uranus, and Neptune. *Icarus* **62**, 425–432.
- NEFF, J. S., D. C. HUMM, J. T. BERGSTRALH, A. L. COCHRAN, W. D. COCHRAN, E. S. BARKER, AND R. G. TULL 1984. Absolute spectrophotometry of Titan, Uranus, and Neptune: 3500–10,500 Å. *Icarus* **60**, 221–235.
- PODOLAK, M., AND L. P. GIVER 1979. On inhomogeneous scattering models of Titan's atmosphere. *Icarus* **37**, 361–376.
- POLLACK, J. B. 1973. Greenhouse models of the atmosphere of Titan. *Icarus* **19**, 43–58.
- POLLACK, J. B., AND C. P. MCKAY 1985. The impact of polar stratospheric clouds on the heating rates of the winter polar stratosphere. *J. Atmos. Sci.* **42**, 245–262.
- POLLACK, J. B., K. RAGES, K. H. BAINES, J. T. BERGSTRALH, D. WENKERT, AND G. E. DANIELSON 1986. Estimates of the bolometric albedos and radiation of Uranus and Neptune. *Icarus* **65**, 442–466.
- POLLACK, J. B., K. RAGES, O. B. TOON, AND Y. L. YUNG 1980. On the relationship between secular brightness changes of Titan and solar variability. *Geophys. Res. Lett.* **7**, 829–832.
- RAGES, K., AND J. B. POLLACK 1979. Titan aerosols: Optical properties and vertical distribution. *Icarus* **41**, 119–130.
- RAGES, K., AND J. B. POLLACK 1983. Vertical distribution of scattering hazes in Titan's upper atmosphere. *Icarus* **55**, 50–62.
- RAGES, K., J. B. POLLACK, AND P. H. SMITH 1983. Size estimates of Titan's aerosols based on Voyager high-phase-angle images. *J. Geophys. Res.* **88**, 8721–8728.
- REID, R. C., J. M. PRAUSNITZ, AND T. K. SHERWOOD 1977. *The Properties of Gases and Liquids*. McGraw-Hill, New York.
- SAGAN, C., AND W. R. THOMPSON 1984. Production and condensation of organic gases in the atmosphere of Titan. *Icarus* **59**, 133–161.
- SAMUELSON, R. E. 1967. Greenhouse effect in semi-infinite atmospheres: Application to Venus. *Astrophys. J.* **147**, 782–798.
- SAMUELSON, R. E. 1983. Radiative equilibrium model of Titan's atmosphere. *Icarus* **53**, 364–387.
- SAMUELSON, R. E., R. A. HANEL, V. G. KUNDE, AND W. C. MAGUIRE 1981. Mean molecular weight and hydrocarbon abundance of Titan's atmosphere. *Nature* **292**, 688–693.
- THOMPSON, W. R., AND C. SAGAN 1984. Titan: Far-infrared and microwave remote sensing of methane clouds and organic haze. *Icarus* **60**, 236–259.
- TOMASKO, M. G., AND P. H. SMITH 1982. Photometry and polarimetry of Titan: Pioneer 11 observations and their implications for aerosol properties. *Icarus* **51**, 65–95.
- TOON, O. B., C. P. MCKAY, T. P. ACKERMAN, AND K. SANTHANAM 1989. Rapid calculation of radiative heating rates and photodissociation rates in inhomogeneous multiple scattering atmospheres. *J. Geophys. Res.*, in press.
- TOON, O. B., C. P. MCKAY, R. COURTIN, AND T. P. ACKERMAN 1988. Methane rain on Titan. *Icarus* **75**, 255–284.
- TOON, O. B., J. B. POLLACK, AND C. SAGAN 1977. Physical properties of the particles composing the Martian dust storm of 1971–1972. *Icarus* **30**, 663–696.
- TOON, O. B., R. P. TURCO, AND J. B. POLLACK 1980. A physical model of Titan's clouds. *Icarus* **43**, 260–282.
- TURCO, R. P., O. B. TOON, R. C. WHITTEN, R. G. KEESEE, AND D. HOLLENBACH 1982. Noctilucent clouds: Simulation studies of their genesis, properties and global influences. *Planet. Space Sci.* **30**, 1147–1181.
- WEST, R. A., A. L. LANE, H. HART, K. E. SIMMONS, C. W. HORD, D. L. COFFEEN, L. W. ESPOSITO, M. SATO, AND R. B. POMPHREY 1983. Voyager 2 photopolarimeter observations of Titan. *J. Geophys. Res.* **88**, 8699–8708.
- YUNG, Y. L., M. ALLEN, AND J. P. PINTO 1984. Photochemistry of the atmosphere of Titan: Comparison between model and observations. *Astrophys. J. Suppl.* **55**, 465–506.
- ZIEGLER, W. T. 1959. The vapor pressures of some hydrocarbons in the liquid and solid state at low temperatures. National Bureau of Standards Technical Note PB-151 363 NTIS 1-18, Washington, DC.